The Astrophysical Journal Supplement Series, 195:10 (31pp), 2011 July doi:10.1088/0067-0049/195/1/10
© 2011. The American Astronomical Society. All rights reserved. Printed in the U.S.A.

THE CHANDRA DEEP FIELD-SOUTH SURVEY: 4 Ms SOURCE CATALOGS

Y. Q. Xue[1,2], B. Luo[1,2], W. N. Brandt[1,2], F. E. Bauer[3,4], B. D. Lehmer[5,6], P. S. Broos[1], D. P. Schneider[1], D. M. Alexander[7], M. Brusa[8,9], A. Comastri[10], A. C. Fabian[11], R. Gilli[10], G. Hasinger[12], A. E. Hornschemeier[13], A. Koekemoer[14], T. Liu[15,16], V. Mainieri[17], M. Paolillo[18], D. A. Rafferty[19], P. Rosati[17], O. Shemmer[20], J. D. Silverman[21], I. Smail[22], P. Tozzi[15], and C. Vignali[23]

[1] Department of Astronomy and Astrophysics, Pennsylvania State University, University Park, PA 16802, USA; xuey@astro.psu.edu
[2] Institute for Gravitation and the Cosmos, Pennsylvania State University, University Park, PA 16802, USA
[3] Pontificia Universidad Católica de Chile, Departamento de Astronomía y Astrofísica, Casilla 306, Santiago 22, Chile
[4] Space Science Institute, 4750 Walnut Street, Suite 205, Boulder, CO 80301, USA
[5] The Johns Hopkins University, Homewood Campus, Baltimore, MD 21218, USA
[6] NASA Goddard Space Flight Centre, Code 662, Greenbelt, MD 20771, USA
[7] Department of Physics, Durham University, Durham, DH1 3LE, UK
[8] Max-Planck-Institut für Extraterrestrische Physik, Giessenbachstrasse, D-85748 Garching, Germany
[9] Department of Astronomy, University of Maryland, Baltimore County, 1000 Hilltop Circle, Baltimore, MD 21250, USA
[10] INAF–Osservatorio Astronomico di Bologna, Via Ranzani 1, Bologna, Italy
[11] Institute of Astronomy, Madingley Road, Cambridge, CB3 0HA, UK
[12] Max-Planck-Institut für Plasmaphysik, Boltzmannstrasse 2, D-85748 Garching, Germany
[13] Laboratory for X-ray Astrophysics, NASA Goddard Space Flight Center, Code 662, Greenbelt, MD 20771, USA
[14] Space Telescope Science Institute, 3700 San Martin Drive, Baltimore, MD 21218, USA
[15] INAF–Osservatorio Astronomico di Trieste, Via Tiepolo 11, I-34131 Trieste, Italy
[16] CAS Key Laboratory for Research in Galaxies and Cosmology, Department of Astronomy, University of Science and Technology of China, Hefei, Anhui 230026, China
[17] European Southern Observatory, Karl-Schwarzschild-Strasse 2, Garching D-85748, Germany
[18] Dipartimento di Scienze Fisiche, Università Federico II di Napoli, Via Cinthia, 80126 Napoli, Italy
[19] Leiden Observatory, Leiden University, Oort Gebouw, P.O. Box 9513 RA, Leiden, The Netherlands
[20] Department of Physics, University of North Texas, Denton, TX 76203, USA
[21] Institute for the Physics and Mathematics of the Universe (IPMU), University of Tokyo, Kashiwanoha 5-1-5, Kashiwa-shi, Chiba 277-8568, Japan
[22] Institute of Computational Cosmology, Durham University, Durham, DH1 3LE, UK
[23] Universitá di Bologna, Via Ranzani 1, Bologna, Italy
Received 2011 January 21; accepted 2011 May 24; published 2011 June 29

ABSTRACT

We present source catalogs for the 4 Ms Chandra Deep Field-South (CDF-S), which is the deepest *Chandra* survey to date and covers an area of 464.5 arcmin^2. We provide a main *Chandra* source catalog, which contains 740 X-ray sources that are detected with WAVDETECT at a false-positive probability threshold of 10^{-5} in at least one of three X-ray bands (0.5–8 keV, full band; 0.5–2 keV, soft band; and 2–8 keV, hard band) and also satisfy a binomial-probability source-selection criterion of $P < 0.004$ (i.e., the probability of sources not being real is less than 0.004); this approach is designed to maximize the number of reliable sources detected. A total of 300 main-catalog sources are new compared to the previous 2 Ms CDF-S main-catalog sources. We determine X-ray source positions using centroid and matched-filter techniques and obtain a median positional uncertainty of $\approx 0\farcs42$. We also provide a supplementary catalog, which consists of 36 sources that are detected with WAVDETECT at a false-positive probability threshold of 10^{-5}, satisfy the condition of $0.004 < P < 0.1$, and have an optical counterpart with $R < 24$. Multiwavelength identifications, basic optical/infrared/radio photometry, and spectroscopic/photometric redshifts are provided for the X-ray sources in the main and supplementary catalogs. Seven hundred sixteen (≈97%) of the 740 main-catalog sources have multiwavelength counterparts, with 673 (≈94% of 716) having either spectroscopic or photometric redshifts. The 740 main-catalog sources span broad ranges of full-band flux and 0.5–8 keV luminosity; the 300 new main-catalog sources span similar ranges although they tend to be systematically lower. Basic analyses of the X-ray and multiwavelength properties of the sources indicate that >75% of the main-catalog sources are active galactic nuclei (AGNs); of the 300 new main-catalog sources, about 35% are likely normal and starburst galaxies, reflecting the rise of normal and starburst galaxies at the very faint flux levels uniquely accessible to the 4 Ms CDF-S. Near the center of the 4 Ms CDF-S (i.e., within an off-axis angle of 3′), the observed AGN and galaxy source densities have reached 9800^{+1300}_{-1100} deg^{-2} and 6900^{+1100}_{-900} deg^{-2}, respectively. Simulations show that our main catalog is highly reliable and is reasonably complete. The mean backgrounds (corrected for vignetting and exposure-time variations) are 0.063 and 0.178 counts Ms^{-1} pixel^{-1} (for a pixel size of $0\farcs492$) for the soft and hard bands, respectively; the majority of the pixels have zero background counts. The 4 Ms CDF-S reaches on-axis flux limits of $\approx 3.2 \times 10^{-17}$, 9.1×10^{-18}, and 5.5×10^{-17} erg cm^{-2} s^{-1} for the full, soft, and hard bands, respectively. An increase in the CDF-S exposure time by a factor of ≈2–2.5 would provide further significant gains and probe key unexplored discovery space.

Key words: cosmology: observations – diffuse radiation – galaxies: active – surveys – X-rays: galaxies

Online-only material: color figures, extended figures, machine-readable tables

1. INTRODUCTION

Deep X-ray surveys indicate that the cosmic X-ray background (CXRB) is largely due to accretion onto supermassive black holes integrated over cosmic time. One of the greatest legacies of the *Chandra X-ray Observatory* is the characterization of the CXRB sources thanks to its extraordinary sensitivity. The Chandra Deep Field-North and Chandra Deep Field-South (CDF-N and CDF-S, jointly CDFs) are the two deepest *Chandra* surveys (see Brandt & Hasinger 2005 and Brandt & Alexander 2010 for reviews of deep extragalactic X-ray surveys), each covering ≈450 arcmin^2 areas with tremendous multiwavelength observational investments. Most of the CDF sources are active galactic nuclei (AGNs), often obscured, at $z \approx 0.1$–5.2. The CDFs have found the highest density of reliably identified AGNs on the sky, with an AGN source density approaching 10,000 sources per deg^2 (e.g., Bauer et al. 2004). At faint fluxes, the CDFs are also detecting large numbers of starburst and normal galaxies at $z \approx 0.1$–2 as well as a few individual off-nuclear X-ray binaries at $z \approx 0.05$–0.3.

Deeper X-ray observations not only further improve the photon statistics that are required to understand better the already detected sources via X-ray spectral and variability constraints, but also probe further down the X-ray luminosity versus redshift plane to characterize better the properties and evolution of typical AGNs and galaxies. The recent extension of the CDF-S survey from 2 Ms (Luo et al. 2008, hereafter L08) to 4 Ms of exposure, via a large Director's Discretionary Time project, has now provided our most sensitive 0.5–8 keV view of the distant universe. These data, complemented by the recent ≈3.3 Ms *XMM-Newton* observations in the CDF-S (Comastri et al. 2011), will enable detailed studies of AGN evolution, physics, and ecology as well as the X-ray properties of normal and starburst galaxies, groups and clusters of galaxies, large-scale structures, and Galactic stars.

In this paper, we present *Chandra* source catalogs and data products derived from the full 4 Ms CDF-S data set as well as details of the observations, data reduction, and technical analysis. We have made a number of methodological improvements in catalog production relative to past CDF catalogs. The structure of this paper is the following: in Section 2 we describe the observations and data reduction; in Section 3 we detail the production of images, exposure maps, and the candidate-list catalog; in Sections 4 and 5 we present the main and supplementary source catalogs as well as description of the adopted methodology, respectively; in Section 6 we perform simulations to assess the completeness and reliability of the main source catalog; in Section 7 we estimate the background and sensitivity across the CDF-S and investigate the prospects for longer CDF-S exposures; and in Section 8 we summarize the results of this work.

Throughout this paper, we adopt a Galactic column density of $N_{\rm H} = 8.8 \times 10^{19}$ cm^{-2} (e.g., Stark et al. 1992) along the line of sight to the CDF-S. We use J2000.0 coordinates and a cosmology of $H_0 = 70.4$ km s^{-1} Mpc^{-1}, $\Omega_{\rm M} = 0.272$, and $\Omega_\Lambda = 0.728$ (e.g., Komatsu et al. 2011).

2. OBSERVATIONS AND DATA REDUCTION

2.1. Observations and Observing Conditions

Table 1 summarizes the basic information for the 31 CDF-S observations that were taken between 2010 March 18 and 2010 July 22, which comprise the second 2 Ms exposure. The first 2 Ms exposure consisted of 23 observations (see Table 1 of L08 for basic information) that were performed between 1999 October 15 and 2007 November 4; the corresponding source catalogs were presented in L08.

All 54 CDF-S observations made use of the Advanced CCD Imaging Spectrometer imaging array (ACIS-I; Garmire et al. 2003). The ACIS-I is comprised of four 1024 × 1024 pixel CCDs (CCDs I0–I3; each has a pixel size of 0.″492) and is optimized for imaging wide fields (with a field of view of $16.'9 \times 16.'9 = 285.6$ arcmin^2). The focal-plane temperature was −110°C during the first two observations (1431-0 and 1431-1; Giacconi et al. 2002; L08) and −120°C during the others. The 10 early CDF-S observations between 1999 November 23 and 2000 December 23 were taken in Faint mode (Giacconi et al. 2002; L08); all the later CDF-S observations as well as the earliest one (observation 1431-0) were taken in Very Faint mode in order to improve the screening of background events and thus increase the sensitivity of ACIS in detecting faint X-ray sources (Vikhlinin 2001).

We inspected the background light curves for all 54 CDF-S observations using the *Chandra* Imaging and Plotting System (ChIPS)[24] as well as EVENT BROWSER in the Tools for ACIS Real-time Analysis (TARA; Broos et al. 2000) software package.[25] We find no significant flaring for all observations (the background is stable within ≈20% of typical quiescent *Chandra* values) except observation 1431-0, during which a mild flare with a factor of ≈3 increase for ≈5 ks occurred. We filtered the data on good-time intervals, removed the one mild flare, and obtained a total exposure time of 3.872 Ms for the 54 CDF-S observations.

The entire CDF-S covers an area of 464.5 arcmin^2; this is considerably larger than the ACIS-I field of view because the aim points and roll angles vary between observations. The average aim point, weighted using the 54 individual exposure times, is $\alpha_{\rm J2000.0} = 03^{\rm h}32^{\rm m}28\overset{\rm s}{.}06$, $\delta_{\rm J2000.0} = -27°48'26.''4$.

2.2. Data Reduction

Table 1 lists the versions of the *Chandra* X-ray Center (CXC) pipeline software used to process the basic archive data products for the 31 new observations (see Table 1 of L08 for the information for the first 23 observations). We closely followed L08 in reducing and analyzing the data and refer readers to L08 for details. Briefly, we utilized *Chandra* Interactive Analysis of Observations (CIAO; we used CIAO 4.2 and CALDB 4.3.0) tools and custom software, including the TARA package (version released on 2010 February 26), as appropriate.

We reprocessed each level 1 observation with the CIAO tool ACIS_PROCESS_EVENTS to correct for the radiation damage sustained by the CCDs during the first few months of *Chandra* operations using a charge transfer inefficiency (CTI) correction procedure (Townsley et al. 2000, 2002),[26] to remove the standard pixel randomization which causes point spread function (PSF) blurring, and to apply a modified bad-pixel file. We made use of a customized stripped-down bad-pixel file rather than the standard CXC bad-pixel file because the latter excludes ≈6%–7% of the ACIS-I pixels on which a large fraction of events are valid for

[24] See http://cxc.harvard.edu/ciao3.4/download/doc/chips_manual/ for the ChIPS reference manual.
[25] TARA is available at http://www.astro.psu.edu/xray/docs/TARA/.
[26] The CXC CTI correction procedure is only available for −120°C data and is thus not applied to observations 1431-0 and 1431-1.

Table 1
Journal of New Chandra Deep Field-South Observations

Obs. ID	Obs. Start (UT)	Exposure Time[a] (ks)	Aim Point[b] α (J2000.0)	Aim Point[b] δ (J2000.0)	Roll Angle[c] (deg)	Pipeline Version[d]
(The 23 observations made during the first 2 Ms exposure are listed in Table 1 of L08)						
12043	2010 Mar 18, 01:39	129.6	03 32 28.78	−27 48 52.1	252.2	8.2.1
12123	2010 Mar 21, 08:08	24.8	03 32 28.78	−27 48 52.1	252.2	8.2.1
12044	2010 Mar 23, 11:31	99.5	03 32 28.55	−27 48 51.9	246.2	8.2.1
12128	2010 Mar 27, 13:08	22.8	03 32 28.55	−27 48 51.9	246.2	8.2.1
12045	2010 Mar 28, 16:38	99.7	03 32 28.32	−27 48 51.4	240.2	8.2.1
12129	2010 Apr 3, 15:21	77.1	03 32 28.33	−27 48 51.4	240.2	8.2.1
12135	2010 Apr 6, 09:36	62.5	03 32 28.01	−27 48 50.2	231.7	8.2.1
12046	2010 Apr 8, 08:17	78.0	03 32 28.01	−27 48 50.2	231.7	8.2.1
12047	2010 Apr 12, 13:21	10.1	03 32 27.80	−27 48 48.9	225.2	8.2.1
12137	2010 Apr 16, 08:53	92.8	03 32 27.59	−27 48 47.2	219.2	8.2.1
12138	2010 Apr 18, 12:40	38.5	03 32 27.59	−27 48 47.3	219.2	8.2.1
12055	2010 May 15, 17:15	80.7	03 32 26.72	−27 48 32.3	181.4	8.2.1
12213	2010 May 17, 14:22	61.3	03 32 26.69	−27 48 31.1	178.9	8.2.1
12048	2010 May 23, 07:09	138.1	03 32 26.64	−27 48 27.6	171.9	8.2.1
12049	2010 May 28, 18:58	86.9	03 32 26.61	−27 48 24.4	165.5	8.2.1
12050	2010 Jun 3, 06:47	29.7	03 32 26.61	−27 48 21.7	160.2	8.2.1
12222	2010 Jun 5, 02:47	30.6	03 32 26.61	−27 48 21.7	160.2	8.2.1
12219	2010 Jun 6, 16:30	33.7	03 32 26.61	−27 48 21.7	160.2	8.2.1
12051	2010 Jun 10, 11:30	57.3	03 32 26.63	−27 48 19.2	155.2	8.2.1
12218	2010 Jun 11, 10:18	88.0	03 32 26.63	−27 48 19.2	155.2	8.2.1
12223	2010 Jun 13, 00:57	100.7	03 32 26.63	−27 48 19.2	155.2	8.2.1
12052	2010 Jun 15, 16:02	110.4	03 32 26.70	−27 48 14.5	145.7	8.2.1
12220	2010 Jun 18, 12:55	48.1	03 32 26.70	−27 48 14.5	145.7	8.2.1
12053	2010 Jul 5, 03:12	68.1	03 32 27.02	−27 48 06.0	127.0	8.3
12054	2010 Jul 9, 11:35	61.0	03 32 27.02	−27 48 06.1	127.0	8.3
12230	2010 Jul 11, 03:52	33.8	03 32 27.02	−27 48 06.0	127.0	8.3
12231	2010 Jul 12, 03:22	24.7	03 32 27.16	−27 48 03.6	121.2	8.3
12227	2010 Jul 14, 21:04	54.3	03 32 27.16	−27 48 03.7	121.2	8.3
12233	2010 Jul 16, 10:25	35.6	03 32 27.16	−27 48 03.7	121.2	8.3
12232	2010 Jul 18, 19:53	32.9	03 32 27.16	−27 48 03.7	121.2	8.3
12234	2010 Jul 22, 19:58	49.1	03 32 27.19	−27 48 03.3	120.2	8.3

Notes. The 4 Ms CDF-S consists of 54 observations, with the first 2 Ms exposure composed of 23 observations (listed in Table 1 of L08; not listed here to avoid repetition) and the second 2 Ms exposure composed of 31 observations (listed in this table; these 31 observations were all taken with the Very Faint mode). Right ascension has units of hours, minutes, and seconds, and declination has units of degrees, arcminutes, and arcseconds.

[a] Each of the 54 observations was continuous. We filtered the data on good-time intervals and removed one mild flare in observation 1431-0 (during the first 2 Ms exposure). The summed exposure time for the 54 observations is 3.872 Ms.

[b] The aim points of the individual observations are the nominal ones taken from the *Chandra* archive. The average aim point, weighted by the 54 exposure times, is $\alpha_{J2000.0} = 03^h32^m28\overset{s}{.}06$, $\delta_{J2000.0} = -27°48'26\overset{''}{.}4$.

[c] Roll angle, describing the orientation of the *Chandra* instruments on the sky, ranges from 0° to 360° and increases to the west of north (opposite to the sense of traditional position angle).

[d] The version of the CXC pipeline software used for the basic processing of the data.

source searching as well as photometry and spectral analysis (see Section 2.2 of L08 for details). Our bad-pixel screening removed ≈1.3% of all events. When cleaning background events, we set CHECK_VF_PHA=YES in ACIS_PROCESS_EVENTS for observations taken in Very Faint mode to utilize a 5 × 5 pixel event island to search for potential cosmic-ray background events, which typically removes ≈20%–30% of the events of individual observations.

We used the CIAO tool ACIS_DETECT_AFTERGLOW to remove cosmic-ray afterglows, which is more stringent than the CIAO tool ACIS_RUN_HOTPIX that often fails to flag a substantial number of obvious cosmic-ray afterglows. Even ACIS_DETECT_AFTERGLOW fails to reject all afterglows. Working in CCD coordinates, we therefore utilized custom software to clean the data further by removing many additional faint afterglows with three or more total counts occurring within 20 s (or equivalently six consecutive frames) on a pixel.[27] We removed a total of 176 additional faint afterglows across the full 4 Ms data set which, upon inspection, were isolated and not associated with apparent legitimate X-ray sources.

As stated above, one significant deviation of our data reduction from the CXC reduction of the CDF-S data set[28] is implementation of a customized stripped-down bad-pixel file, which retains an appreciable number of valid events (accounting for ≈5% of all events) that would have been discarded

[27] As shown later in Table 8, the full-band (i.e., 0.5–8 keV) mean background rate of the 4 Ms CDF-S is 0.252 counts Ms^{-1} pixel^{-1}, which translates into a count rate of 5.04×10^{-6} counts per 20 s per pixel. Given such a low background count rate, the probability of three or more counts (that are not associated with cosmic-ray afterglows) occurring within 20 s on a pixel by chance is negligible (2.54×10^{-11}).

[28] The CXC CDF-S data products are available at http://cxc.harvard.edu/cda/Contrib/CDFS.html.

using the standard CXC bad-pixel file. As will be described in Sections 3.1 and 3.2, when creating the CDF-S data products (e.g., merged X-ray images) and source catalogs (e.g., X-ray source positions), we registered individual X-ray observations to a common optical/radio astrometric frame (see Section 3.1) and refined the absolute astrometry of the merged X-ray images and source positions using high-quality radio data (see Section 3.2), thereby producing sharp merged X-ray images and accurate X-ray source positions (with $<0\farcs2$ astrometric shifts); in contrast, the CXC did not utilize multiwavelength data to register and refine X-ray astrometry.

3. IMAGES, EXPOSURE MAPS, AND CANDIDATE-LIST CATALOG

While following the general procedure described in Section 3 of L08 in the production of our source catalogs, we extensively made use of the ACIS Extract (AE; version released on 2010 February 26; Broos et al. 2010)[29] point-source analysis software that appropriately computes source properties when multiple observations with different roll angles and/or aim points are being combined (such as those analyzed here). Significant improvements from the methodology of L08 include, e.g., (1) utilization of AE polygonal source-count extraction regions that approximate the shape of the PSF and take into account the multi-observation nature of the data, and (2) utilization of a two-stage approach to source detection, which filters candidate sources according to binomial no-source probabilities (i.e., probabilities of sources not being real considering their local backgrounds) calculated by AE.

We first generated a candidate-list catalog of sources detected by WAVDETECT (Freeman et al. 2002) on the combined images (see Section 3.2) at a false-positive probability threshold of 10^{-5}. We then pruned the candidate-list catalog to obtain a more conservative main catalog by removing low-significance source candidates, according to the AE-computed binomial no-source probabilities. As detailed later in Sections 3.2 and 4, this approach not only produces source catalogs that are of similar quality to those produced by running WAVDETECT at the more typical false-positive probability threshold of 10^{-6} or 10^{-7} used in previous CDF studies (e.g., Alexander et al. 2003, hereafter A03; Lehmer et al. 2005, hereafter L05; L08), but also allows for flexibility in including additional legitimate sources that fall below the 10^{-6} or 10^{-7} threshold. This procedure has previously been employed in similar forms in a number of studies (e.g., Getman et al. 2005; Nandra et al. 2005; Laird et al. 2009; Lehmer et al. 2009).

3.1. Image and Exposure Map Creation

To construct the combined event file, we initially ran WAVDETECT at a false-positive probability threshold of 10^{-6} on the individual cleaned 0.5–8 keV image of each observation to generate initial source lists and used AE to determine centroid positions of each detected source. We then registered the observations to a common astrometric frame by matching X-ray centroid positions to optical sources detected in deep *R*-band images taken with the Wide Field Imager (WFI) mounted on the 2.2 m Max Planck Gesellshaft/European Southern Observatory (ESO) telescope at La Silla (see Section 2 of Giavalisco et al. 2004). We have manually shifted all the WFI *R*-band source positions by $0\farcs175$ in right ascension and $-0\farcs284$ in declination (also see Luo et al. 2010, hereafter L10) to remove the systematic offsets between the optical positions and the radio positions of sources in the Very Large Array (VLA) 1.4 GHz radio catalog presented in Miller et al. (2008).[30] We did not directly match X-ray centroid positions to the VLA radio catalog because, for some observations, there are too few common sources between the X-ray and radio source lists to ensure a robust astrometric solution, owing to the relatively low radio source density and relatively small numbers of *Chandra* sources detected in *individual* observations. However, as detailed in Section 3.2, we are able to lock the absolute astrometry of the *combined* X-ray images to the VLA radio catalog because of the larger number of X-ray sources detected. We performed X-ray/*R*-band matching and astrometric re-projection using the CIAO tools REPROJECT_ASPECT and WCS_UPDATE with a $3''$ matching radius and a residual rejection limit[31] of $0\farcs6$. Typically, 60–150 X-ray/*R*-band matches were used in each observation for the astrometric solutions. When using WCS_UPDATE, linear translations range from $0\farcs032$ to $0\farcs525$, rotations range from $-0\fdg048$ to $0\fdg035$, and scale changes range from 1.00004 to 1.00145. Individual registrations are accurate to $\approx 0\farcs3$. We then re-projected all the observations to the frame of observation 2406, which is one of the observations that requires the smallest translation to be aligned with the optical astrometric frame; however, we note that it does not matter which observation is used as the reference frame for re-projection once each observation is analyzed consistently.

We utilized the CIAO tool DMMERGE to produce a merged event file by combining the individual event files. We constructed images from this merged event file using the standard *ASCA* grade set (*ASCA* grades 0, 2, 3, 4, 6) for three standard bands: 0.5–8.0 keV (full band; FB), 0.5–2.0 keV (soft band; SB), and 2–8 keV (hard band; HB).[32] Figure 1 shows the raw full-band image. We generated effective-exposure maps for the three standard bands following the basic procedure outlined in Section 3.2 of Hornschemeier et al. (2001) and normalized them to the effective exposures of a pixel located at the average aim point. This procedure takes into account the effects of vignetting, gaps between the CCDs, bad-column filtering, bad-pixel filtering, and the spatial- and time-dependent degradation in quantum efficiency due to contamination on the ACIS optical-blocking filters; thus, the derived effective exposures are typically smaller than the nominal exposures (i.e., durations of observations). When creating the effective-exposure maps, we assumed a photon index of $\Gamma = 1.4$, the slope of the cosmic 2–10 keV X-ray background (e.g., Marshall et al. 1980; Gendreau et al. 1995; Hasinger et al. 1998; Hickox & Markevitch 2006). Figure 2 shows the full-band effective-exposure map, and Figure 3 displays the survey solid angle as a function of the minimum full-band effective exposure.

[29] See http://www.astro.psu.edu/xray/docs/TARA/ae_users_guide.html for details on ACIS Extract.

[30] Throughout this paper, we used the 5σ VLA 1.4 GHz radio catalog (N. A. Miller 2010, private communication) that has a limiting flux density of $\approx 40\,\mu$Jy.

[31] This is a parameter used in WCS_UPDATE to remove source pairs based on pair positional offsets.

[32] We compared X-ray source catalogs made with the two upper energy cuts of 7 keV and 8 keV (i.e., the set of energy bands of 0.5–7.0, 0.5–2.0, and 2–7 keV versus the set of energy bands adopted here; see Sections 3.2 and 4.1 for the details of catalog production). We found no clear statistical difference between catalogs; the X-ray sources that are unique in each catalog are faint (i.e., close to or right on source-detection limits) and account for only $\approx$3% of all detected sources. We thus adopted the traditional standard bands (i.e., using the upper energy cut of 8 keV) to maintain continuity with past catalogs (e.g., A03; L05; L08).

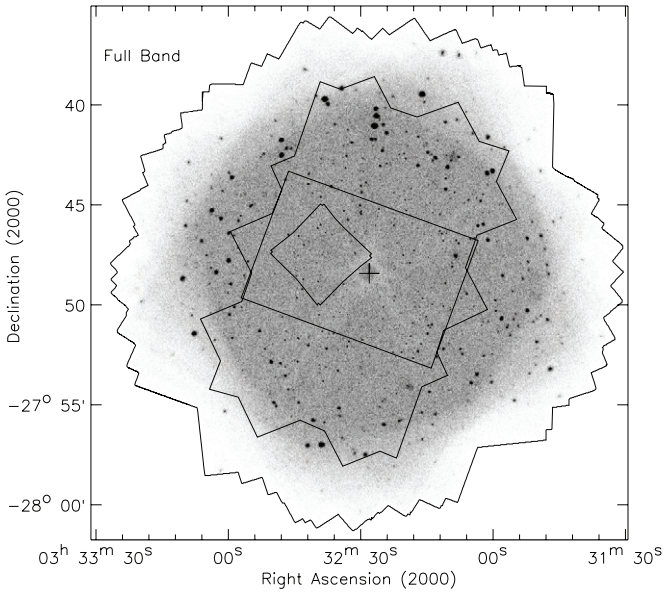

Figure 1. Full-band (0.5–8.0 keV) raw image of the 4 Ms CDF-S displayed with linear gray scales. The segmented boundary surrounding the image shows the coverage of the entire CDF-S. The large polygon, the rectangle, and the central small polygon indicate the regions for the GOODS-S (Giavalisco et al. 2004), the planned CANDELS GOODS-S (5-orbit *HST*/WFC3; see Section 8 for more details about CANDELS), and the Hubble Ultra Deep Field (UDF; Beckwith et al. 2006), respectively. The central plus sign indicates the average aim point, weighted by exposure time (see Table 1). The pale ring-like area near the field center is caused by the ACIS-I CCD gaps in which the effective exposures are lower than in the nearby non-gap areas (see Figure 2). The apparent scarcity of sources near the field center is mainly due to the small size of the on-axis PSF (see Figures 4 and 15 for clarification).

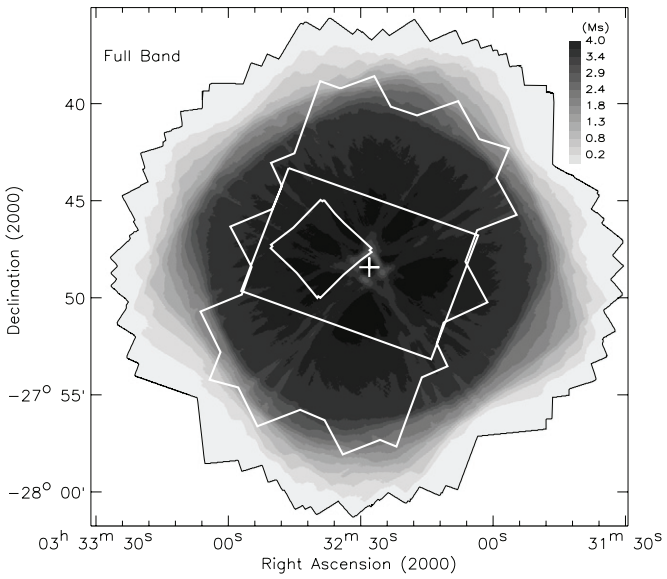

Figure 2. Full-band (0.5–8.0 keV) effective-exposure map of the 4 Ms CDF-S displayed with linear gray scales that are indicated by the inset scale bar (effective exposure times are in units of seconds). The darkest areas represent the highest effective exposure times, with a maximum of 3.811 Ms. The distributions of the ACIS-I CCD gaps can be clearly identified (indicated by the radial trails). The regions and the plus sign are the same as those in Figure 1.

According to Figure 3, about 52% and 38% of the CDF-S field has a full-band effective exposure greater than 2 Ms and 3 Ms, respectively; the maximum effective exposure is 3.811 Ms, which is slightly smaller than the 3.872 Ms total exposure since the locations of the aim points of individual observations vary.

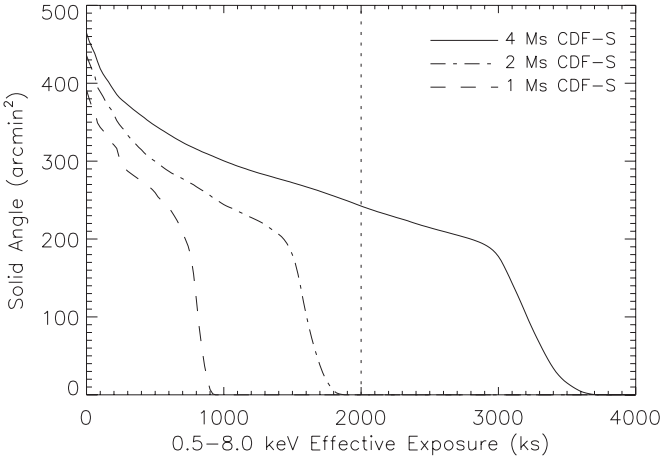

Figure 3. Plot of survey solid angle as a function of minimum full-band effective exposure for the 4 Ms CDF-S (solid curve). The maximum exposure is 3.811 Ms. The vertical dotted line indicates an effective exposure of 2 Ms. Approximately 242.3 arcmin^2 (≈52%) of the CDF-S survey area has >2 Ms effective exposure. For comparison, the 1 Ms CDF-S result (dashed curve) and the 2 Ms CDF-S result (dash-dotted curve), both of which are obtained using the procedures in this paper, are also shown in the plot.

For a given full-band effective exposure, the survey solid angle is up to a factor of ≈1.5 times larger than that of the 2 Ms CDF-S (L08; Figure 3, dash-dotted curve) at the low end of effective exposure (<1.5 Ms), and it is much larger than that of the 2 Ms CDF-S above 1.5 Ms effective exposure. Thus in addition to the fact that the 4 Ms CDF-S can detect new sources that have lower fluxes than the 2 Ms sources, it can also detect new sources that have a similar flux distribution to the 2 Ms sources over as much as 50% more area.

We followed Section 3.3 of Baganoff et al. (2003) to construct exposure-corrected smoothed images. We first produced the raw images and effective-exposure maps in the 0.5–2.0 keV, 2–4 keV, and 4–8 keV bands, using the aforementioned procedures. We then adaptively smoothed the raw images and effective-exposure maps using the CIAO tool CSMOOTH (Ebeling et al. 2006). Finally, we divided the smoothed images by their corresponding smoothed effective-exposure maps and combined the exposure-corrected smoothed images together to produce a full-band color composite, as shown in Figure 4 (note that this color composite is not background-subtracted); an expanded view of the central $8' \times 8'$ region is also shown in Figure 4. Note that we ran WAVDETECT only on the raw images for source searching, although many detected X-ray sources appear more clearly in the adaptively smoothed images.

3.2. Candidate-list Catalog Production

We ran WAVDETECT on each combined raw image in the three standard bands[33] to perform source searching and to construct a candidate-list catalog, using a "$\sqrt{2}$ sequence" of wavelet scales (i.e., 1, $\sqrt{2}$, 2, $2\sqrt{2}$, 4, $4\sqrt{2}$, 8, $8\sqrt{2}$, and 16 pixels) and a false-positive probability threshold of 10^{-5}. We expect the use of a false-positive probability threshold of 10^{-5} to introduce a non-negligible number of spurious sources that have $\lesssim$2–3 source counts. However, as pointed out by Alexander et al. (2001),

[33] We note that WAVDETECT was run on the *combined* raw images where the average aim point (given in Section 2) is a good approximation of the image center for the purpose of computing PSFs. Given that we used multiple wavelet scales, the Mexican-Hat wavelet patterns (adopted by WAVDETECT) provide reasonable first-order approximations of the multi-observation PSFs.

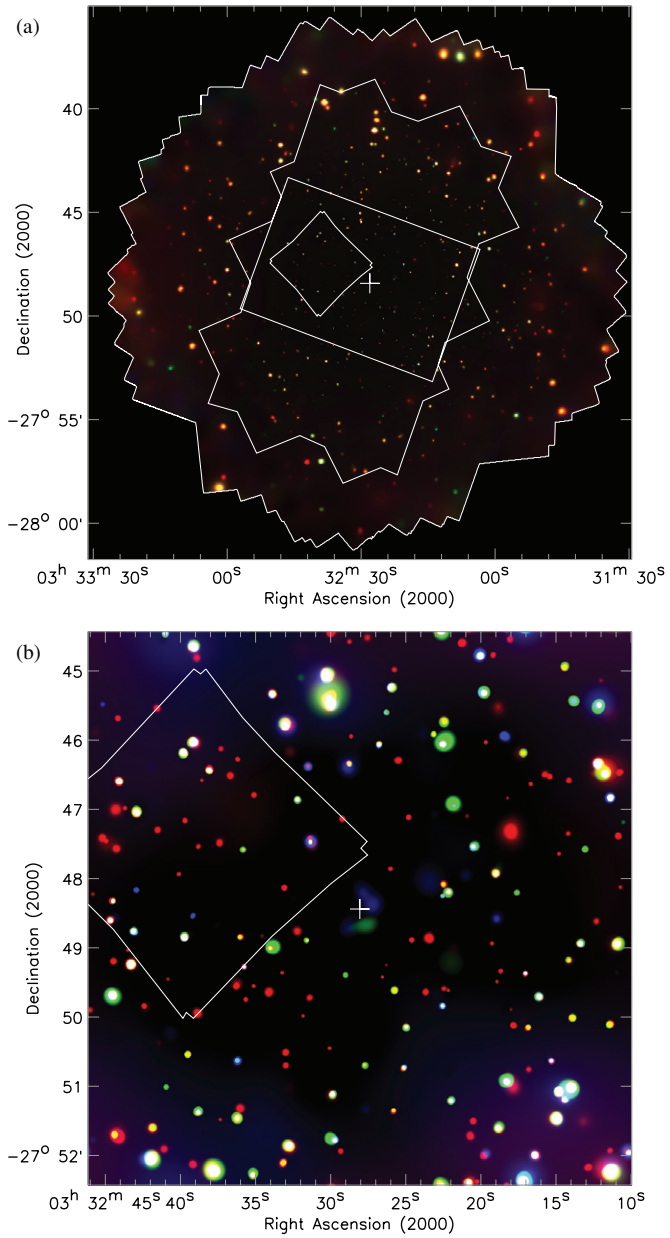

Figure 4. (a) *Chandra* "false-color" image of the 4 Ms CDF-S, which is a color composite of the exposure-corrected and adaptively smoothed images in the 0.5–2.0 keV (red), 2–4 keV (green), and 4–8 keV (blue) bands. (b) An expanded view of the *Chandra* "false-color" image of the central $8' \times 8'$ region (note that a slightly different contrast ratio from that for the full image is used here in order to render the faint sources more clearly). The apparent smaller size and lower brightness of sources near the field center is due to the smaller size of the on-axis PSF. The regions and the plus sign are the same as those in Figure 1.

using a more stringent source-detection threshold (e.g., 10^{-6}, 10^{-7}, or 10^{-8}) can lose an appreciable number of real sources. In Section 4, we create a more conservative main catalog by determining the detection significances of each candidate-list source in the three standard bands and discarding sources with significances below an adopted threshold value.

Our candidate-list catalog consists of 892 X-ray source candidates; each candidate was detected in at least one of the three standard bands with WAVDETECT at a false-positive probability threshold of 10^{-5}. We adopted, in order of priority, full-band, soft-band, or hard-band source positions for candidate sources. We performed cross-band matching using a 2.″5 matching radius for sources within 6′ of the average aim point (i.e., off-axis angle $\theta < 6'$) and a 4.″0 matching radius for sources located at larger off-axis angles (i.e., $\theta \geqslant 6'$). The choice of these matching radii was made based on inspection of histograms that show the number of matches as a function of angular separation (e.g., see Section 2 of Boller et al. 1998). With these matching radii, the mismatch probability is ≈1% over the entire field. We removed a few duplicate sources due to false matches near the edge of the field through visual inspection.[34]

We improved the above WAVDETECT source positions utilizing the centroid and matched-filter positions computed by AE. The matched-filter positions are obtained by correlating the full-band image in the neighborhood around each source with the source's combined PSF. The combined PSF is generated by combining the individual PSFs of a source for each relevant observation, weighted by the number of detected counts. This technique takes into account the fact that, due to the complex PSF at large off-axis angles, the X-ray source position is not always located at the peak of the X-ray emission. The WAVDETECT, centroid, and matched-filter positions have comparable accuracy on-axis, while the matched-filter positions have better accuracy off-axis. Thus, we adopted centroid positions for sources with $\theta < 8'$ and matched-filter positions for sources with $\theta \geqslant 8'$.

We refined the absolute astrometry of the raw X-ray images by matching the candidate-list sources to the 5σ VLA 1.4 GHz radio-catalog sources (see Section 3.1). There are 359 radio sources across the CDF-S field with positions accurate to $\lesssim$0.″1. We performed cross-matching between the 892 candidate-list catalog X-ray sources and the 359 radio sources in the field using a 2″ matching radius and found 141 matches. We estimated the expected false matches by manually shifting the X-ray source positions in right ascension and declination by ±(5″–60″) in steps of 5″ (i.e., in unique directions) and recorrelating with the radio sources. The average number of false matches is ≈2.3 (≈1.7%) and the median offset of these false matches is 1.″41. Of the 141 matches, we identified five extended radio sources upon inspecting the radio image. We excluded two of these five extended radio sources for the astrometry refinement analysis because these two matches are spurious with positional offsets greater than 1.″5 (see Section 4.2 for more details on these two extended radio sources); the other three matches are robust with small positional offsets (<0.″7) and were included for the subsequent analysis. Using these 139 matches, we found small shift and plate-scale corrections when comparing the X-ray and radio source positions and applied these corrections to all the combined X-ray images and source positions, which results in small (<0.″2) astrometric shifts.

We utilized AE to perform photometry for the candidate-list catalog sources. Compared to "traditional" circular-aperture photometry (e.g., L08), the most important difference in the AE-computed photometry is the use of polygonal source-extraction regions.[35] AE models the *Chandra* High Resolution

[34] For a few sources that lie near the edge of the field, the offset between the X-ray positions determined from different bands by WAVDETECT is >4″; such a source will be counted twice (i.e., treated as two sources) according to our matching approach (i.e., a 4.″0 matching radius at $\theta \geqslant 6'$). We removed the duplicated sources in these few cases.

[35] The polygonal source-extraction regions typically become more non-circular toward larger off-axis angles. In particular, the source-extraction regions for crowded sources at large off-axis angles are reduced from ≈90% to ≈40%–75% encircled-energy fractions (EEFs) and thus represent the most dramatic examples of deviation from circular apertures (see, e.g., Figure 6 of Broos et al. 2010 for such an example).

Mirror Assembly using the MARX[36] ray-tracing simulator (version 4.4.0) to obtain the PSF model. It then constructs a polygonal extraction region that approximates the ≈90% encircled-energy fraction (EEF) contour of a local PSF measured at 1.497 keV (note that AE also constructs PSFs at energies of 0.277, 4.510, 6.400, and 8.600 keV). When dealing with crowded sources having overlapping polygonal extraction regions, AE utilized smaller extraction regions (corresponding to ≈40%–75% EEFs) that were chosen to be as large as possible without overlapping. Less than 6% of the 892 candidate-list sources are crowded by this definition. For background extraction, we adopted the AE "BETTER_BACKGROUNDS" algorithm. This algorithm models the spatial distributions of flux for the source of interest and its neighboring sources using unmasked data. It then computes local background counts within background regions that subtract contributions from the source and its neighboring sources. In our AE usage, the background-extraction region is typically a factor of ≈16 larger than the source-extraction region and contains at least 100 background counts. As discussed in Section 7.15 of the AE manual, AE also imposes an explicit requirement that the uncertainty in the estimate of net counts be dominated by the uncertainty in the extracted source counts in order to ensure photometric accuracy; this requirement leads to enlargement of background regions/counts when necessary. As a result, the median number of full-band background counts extracted for the main-catalog sources (see Section 4.4) is 780, with an interquartile range of 278–2621. This algorithm produces accurate background extractions, which are particularly critical for crowded sources. For sources that are not crowded, this algorithm produces essentially the same background-extraction results as the traditional AE "EXTRACT_BACKGROUNDS" algorithm; the latter algorithm computes local background counts by masking all the sources and then searching around each source for the smallest circular region that contains a desired number of background counts. AE analyzes individual observations independently (including, e.g., the use of MARX for PSF modeling and source and background extractions) and merges the data to produce photometry for each source.[37] The resulting combined PSFs at 1.497 keV have typical FWHMs of 0.″68, 1.″07, 1.″76, 2.″79, and 3.″61 at off-axis angles of 1′, 3′, 5′, 7′, and 9′, respectively; these FWHM values represent typical angular resolutions of the 4 Ms images.

AE estimates an energy-dependent aperture correction for each source and applies the correction to the effective area calibration file used for spectral modeling. For this work, we chose to apply aperture corrections to the background-subtracted photometry as follows. For the soft (hard) band, we derived an effective PSF fraction for each source by weighting PSF measurements at 1.497 (4.510) keV by the exposures for the individual observations. Given that the full band is a combination of the soft and hard bands, we derived the full-band effective PSF fraction based on the derived soft-band and hard-band effective PSF fractions: (1) if a source was detected both in the soft and hard bands, we derived the full-band effective PSF fraction by weighting the soft- and hard-band effective PSF fractions with the soft- and hard-band background-subtracted counts; (2) if a source was detected in the soft or hard band (but not both), we set the full-band effective PSF fraction to the soft- or hard-band effective PSF fraction, respectively; and (3) if a source was detected in neither the soft band nor the hard band, we took the average of the soft- and hard-band effective PSF fractions as the full-band effective PSF fraction. The median aperture corrections for the full, soft, and hard bands are 0.875, 0.898, and 0.826, respectively. We then applied aperture corrections by dividing the background-subtracted source counts by the derived effective PSF fractions. Since our candidate-list catalog was constructed using WAVDETECT with a liberal false-positive probability threshold of 10^{-5}, many candidate sources have $\lesssim$2–3 (background-subtracted) source counts. In the next section, we evaluate the reliability of candidate sources on a source-by-source basis to produce a more robust main source catalog.

4. MAIN *CHANDRA* SOURCE CATALOG

4.1. Selection of Main-catalog Sources

As discussed above, we expect our candidate-list catalog of 892 X-ray sources to include a significant number of false sources since we ran WAVDETECT at a liberal false-positive probability threshold of 10^{-5}. If we conservatively treat the three standard-band images as independent, we can estimate the number of expected false sources in the candidate-list catalog for the case of a uniform background by multiplying the WAVDETECT threshold of 10^{-5} by the sum of pixels in the three bands (i.e., $\approx 2.07 \times 10^7$). However, such a false-source estimate is conservative, since over the majority of the field, a single pixel will not be considered a source-detection cell. In particular, at large off-axis angles WAVDETECT suppresses fluctuations on scales smaller than the PSF. As quantified in Section 3.4.1 of A03, the number of false sources is likely ≈2–3 times smaller than the above conservative estimate. We refer readers to Section 6.2 for relevant discussions.

To produce a more reliable main *Chandra* source catalog, we evaluated for each source the binomial probability P that no source exists given the measurements of the source and local background. As discussed in Section 5.10.3 of the AE manual (also see Appendix A2 of Weisskopf et al. 2007 for further details), the binomial no-source probability P can be calculated using the following equation:

$$P(X \geqslant S) = \sum_{X=S}^{N} \frac{N!}{X!(N-X)!} p^X (1-p)^{N-X}. \quad (1)$$

In this equation, S is the total number of counts in the source-extraction region without subtraction of the background counts $B_{\rm src}$ in this region; $N = S + B_{\rm ext}$, where $B_{\rm ext}$ is the total extracted background counts within a background-extraction region that is typically a factor of ≈16 larger than the source-extraction region in our AE usage (see Section 3.2); and $p = 1/(1+BACKSCAL)$ is the probability that a photon lies in the source-extraction region (thus contributing to S), where $BACKSCAL = B_{\rm ext}/B_{\rm src}$ with a typical value of ≈16, as stated earlier. P is computed by AE in each of the three standard bands. For a source to be included in our main catalog, we required $P < 0.004$ in at least one of the three standard bands. We identified multiwavelength counterparts for the X-ray sources (see Section 4.3) and studied the identification rate as a function of the P value, given that X-ray sources without identifications in ultradeep multiwavelength data are more likely to be false detections (see, e.g., L10). The requirement of $P < 0.004$ was empirically chosen as a

[36] MARX is available at http://space.mit.edu/CXC/MARX/index.html.

[37] For this work, we did not use the optional AE "MERGE_FOR_PHOTOMETRY" algorithm, as discussed in Broos et al. (2010), that allows AE to discard some extractions during a merge of AE products from individual observations.

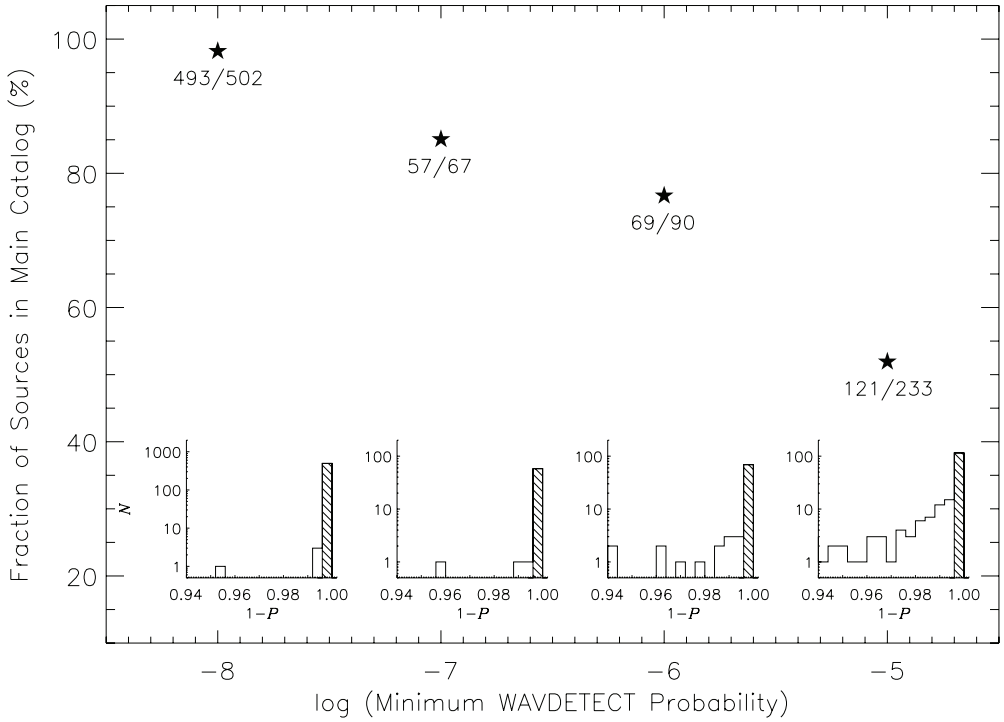

Figure 5. Fraction of sources in the candidate-list catalog with an AE binomial no-source probability $P < 0.004$, which were included in the main catalog, as a function of minimum WAVDETECT probability[38] (shown as five-pointed stars). The number of sources with $P < 0.004$ vs. the number of candidate-list catalog sources detected at each minimum WAVDETECT probability are annotated in the figure (note that, in this figure, 502+67+90+233=892 and 493+57+69+121=740). The fraction of candidate-list catalog sources included in the main catalog fall from 98.2% to 51.9% between minimum WAVDETECT probabilities of 10^{-8} and 10^{-5}. Shown in the insets are the histograms of $1 - P$ for the candidate-list catalog sources at each minimum WAVDETECT probability, with shaded areas highlighting those included in the main catalog (i.e., having $1 - P > 0.996$).

compromise to keep the fraction of potential false sources small while recovering the largest number of real sources. Using this criterion of $P < 0.004$, our main catalog contains a total of 740 sources. We note that for a different choice of source-detection criterion of $P < 0.01$, a total of 33 additional sources with $0.004 \leqslant P < 0.01$ would be included; however, only ≈64% (i.e., 21) of these 33 sources have multiwavelength counterparts, as opposed to an identification rate of ≈97% for the main catalog (see Section 4.3). We refer readers to Section 6.2 for a detailed discussion on the completeness and reliability of the main catalog based on simulations.

Our adopted cataloging procedure, with the utilization of AE, has a number of advantages over a "traditional" WAVDETECT-only approach: (1) the more detailed treatment of complex source-extraction regions (i.e., using polygonal regions, as opposed to elliptical apertures, to simulate the PSF) that is more suitable for the case of multiple observations with different aim points and roll angles, (2) the better source-position determination that maximizes the signal-to-noise ratio and leads to more accurate count estimates, (3) the more careful background estimates that take into account the effects of all the neighboring sources and CCD gaps, and (4) the more immediately transparent mathematical criterion (i.e., the binomial probability) that is utilized for source detection. We will demonstrate below that our adopted procedure recovers almost all of the sources detected with WAVDETECT at a false-positive probability threshold of 10^{-6} and a significant number of additional real sources detected at 10^{-5}.

In order to give a more detailed WAVDETECT-based perspective on source significance, we also ran WAVDETECT on the three standard-band images at false-positive probability thresholds of 10^{-6}, 10^{-7}, and 10^{-8}, and found detections for 659 (73.9%), 569 (63.8%), and 502 (56.3%) of the 892 candidate-list catalog sources, respectively. Among the 152 candidate-list sources that failed the selection cut of $P < 0.004$, and thus were not included in the main catalog, 40 (≈4.5% of the 892 candidate-list sources) had WAVDETECT false-positive probability detection thresholds of $\leqslant 10^{-6}$. Meanwhile, our main catalog includes 121 sources that had minimum WAVDETECT probabilities of 10^{-5}.[38] Therefore, our adopted procedure, as opposed to a direct WAVDETECT-based approach, has a "net gain" of 81 sources. We note that a larger net gain of sources could be achieved if we adopted a less conservative no-source probability cut (e.g., $P < 0.01$) at the expense of introducing more spurious sources.

Figure 5 shows the fraction of candidate-list sources included in the main catalog and the $1 - P$ distribution of candidate-list sources as a function of the minimum WAVDETECT probability. The fraction of candidate-list sources included in the main catalog is 98.2%, 85.1%, 76.7%, and 51.9% for a minimum WAVDETECT probability of 10^{-8}, 10^{-7}, 10^{-6}, and 10^{-5}, respectively. As shown later in Section 4.3, we find that 716 (96.8%) of the 740 main-catalog sources have secure multiwavelength counterparts (with a false-matching probability of ≈2.1%), where the identification rate is 98.1% (90.1%) for the 619 (121) sources with a minimum WAVDETECT probability of $\leqslant 10^{-6}$ (10^{-5}) in the main catalog. Given the relatively small

[38] The minimum WAVDETECT probability represents the WAVDETECT significance of a source, with lower values indicating higher significances. For example, if a source was detected with WAVDETECT in at least one of the three standard bands at a false-positive probability threshold of 10^{-7} but was not detected in any of the three standard bands at a threshold of 10^{-8}, then the minimum WAVDETECT probability of this source is 10^{-7}.

false-matching rate, the above high identification rates indicate that the vast majority of the main-catalog sources are real X-ray sources (see, e.g., L10). Thus, our main-catalog selection provides an effective identification of real X-ray sources including those falling below the traditional 10^{-6} WAVDETECT searching threshold.

4.2. X-Ray Source Positional Uncertainty

As in Section 3.2, we cross-matched the 740 main-catalog sources with the 359 radio sources in the field using a 2″ matching radius and found 135 matches.[39] We estimated on average ≈2.0 (≈1.5%) false matches and a median offset of 1.″45 for these false matches. Figure 6(a) shows the positional offset between the X-ray sources and their radio counterparts as a function of off-axis angle. The median positional offset is 0.″24. There are three sources in Figure 6(a) that have positional offsets greater than 1.″5: (1) the one with the largest offset (1.″97) mistakenly matches to one of the two lobes of a radio galaxy due to the fact that the radio core, which is likely the real counterpart for this X-ray source, was not detected in the radio catalog; (2) the one with the second largest offset (1.″88) is likely a false match because such an offset is much larger than its expected positional uncertainty (see Equation (2) below) considering its off-axis angle (11.′6) and source counts (≈100); and (3) the one with the third largest offset (1.″62) has one radio source, which is the core of a radio galaxy, and a few optical sources within its 2″ radius, with the radio counterpart not matching to the likely real optical counterpart of this X-ray source (thus being a false match). Excluding the above three sources, we then estimated X-ray positional uncertainties using the remaining 132 X-ray-detected radio sources. Figure 6(b) shows the positional residuals between the X-ray and radio positions for these 132 sources; the "scatter cloud" of positional residual appears circular, with no residual distortions. As shown in Figure 6(a), there are clear off-axis angle and source-count dependencies for these 132 sources, with the former due to the degradation of the *Chandra* PSF at large off-axis angles and the latter due to statistical limitations in finding the centroid of a faint X-ray source. Implementing the parameterization provided by Kim et al. (2007),[40] we derived an empirical relation for the positional uncertainty of our X-ray sources by fitting to these 132 X-ray sources that have radio counterparts within a radius of 1.″5. The relation is

$$\log \Delta_X = 0.0484\theta - 0.4356 \log C + 0.1258, \qquad (2)$$

where Δ_X is the X-ray positional uncertainty in arcseconds, θ is the off-axis angle in arcminutes, and C is the source counts in the energy band where the source position was determined (see the description of Columns 8–16 of the main catalog in Section 4.4 for details on photometry calculation). We set an upper limit of 2000 on C since the positional accuracy does not improve significantly above that level. As a guide to the derived relation, we show positional uncertainties for $C = 20$, 200, and 2000 in Figure 6. The stated positional uncertainties are for the ≈68% confidence level, which are smaller than the WAVDETECT positional uncertainties, particularly at large off-axis angles, due

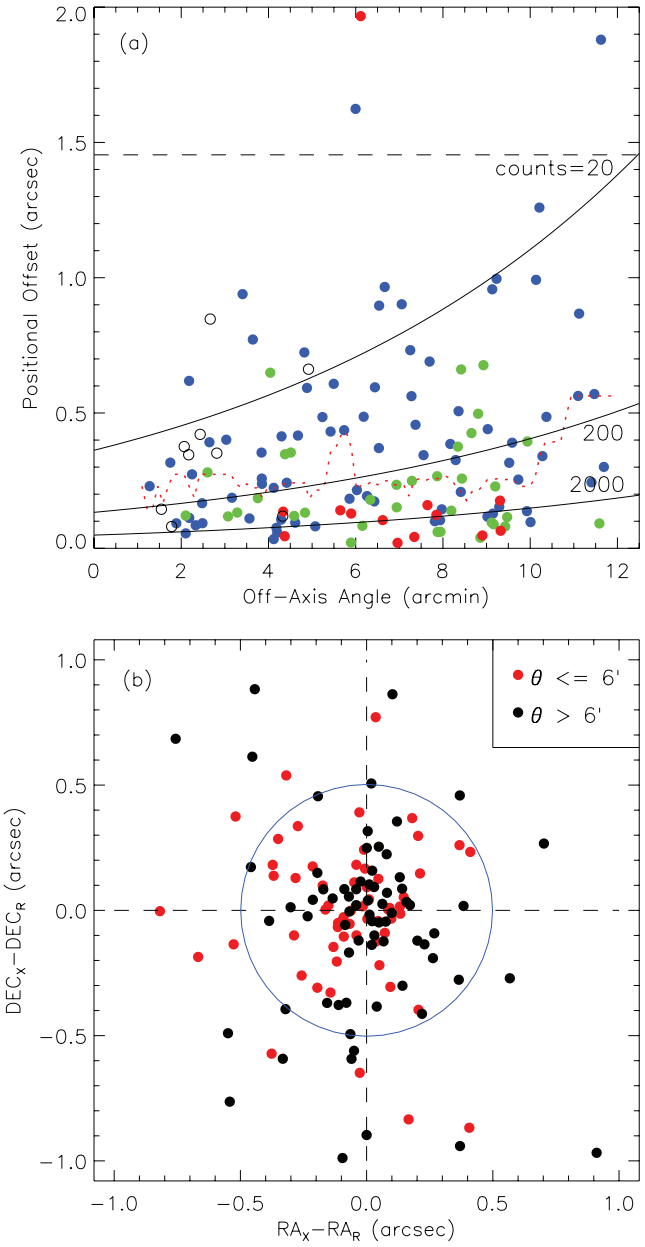

Figure 6. (a) Positional offset vs. off-axis angle for the 135 main-catalog sources that have counterparts in the 5σ VLA 1.4 GHz radio catalog using a matching radius of 2″ (see Section 4.2 for descriptions of the three sources with >1.″5 positional offsets). Red filled, green filled, blue filled, and black open circles represent X-ray sources with ⩾2000, ⩾200, ⩾20, and <20 counts in the energy band where the source position was determined, respectively. The red dotted curve shows the running median of positional offset in bins of 2′. The horizontal dashed line indicates the median offset (1.″45) of the expected false matches. We used these data to derive the ≈68% confidence level X-ray source positional uncertainties, i.e., Equation (2). Three solid curves indicate the ≈68% confidence level positional uncertainties for sources with 20, 200, and 2000 counts. (b) Positional residuals between the X-ray and radio positions for the 132 main-catalog sources that have radio counterparts within a radius of 1.″5 (see panel (a)). Red and black filled circles indicate sources with an off-axis angle of ⩽6′ and >6′, respectively. A large blue circle with a radius of 0.″5 is drawn at the center as a guide to the eyes.

(A color version of this figure is available in the online journal.)

to our adopted positional refinement. In Figure 7, we show the distributions of positional offset in four bins of X-ray positional uncertainty as well as the expected false matches assuming a uniform spatial distribution of radio sources. For each histogram in Figure 7, as expected, ≳65% of the positional offsets between

[39] We note that six (i.e., 141 − 135 = 6; also see Section 3.2) candidate-list X-ray sources that have a radio counterpart were not included in the main catalog; these sources are likely real X-ray sources that fail to satisfy our relatively stringent source-selection criterion of $P < 0.004$ (see Section 4.1).

[40] We note that the Kim et al. (2007) parameterization fits our data adequately (i.e., the AE-derived positions and photometry), although it was originally based on WAVDETECT-derived positions and photometry.

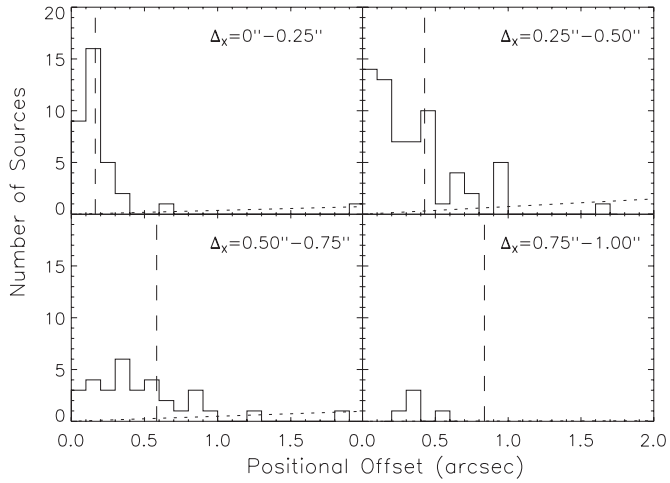

Figure 7. Histograms showing the distributions of positional offset for the 135 main-catalog sources that have counterparts in the 5σ VLA 1.4 GHz radio catalog using a matching radius of 2″. These 135 sources were divided into four bins according to their positional uncertainties estimated using Equation (2): 0″–0.″25, 0.″25–0.″50, 0.″50–0.″75, and 0.″75–1″. The vertical dashed line in each panel indicates the median X-ray positional uncertainty in each bin. The dotted line shows the total expected number of random radio sources as a function of the positional offset. $\lesssim$35% of the radio counterparts lie beyond the median X-ray positional uncertainty in each bin.

the X-ray sources and their radio counterparts are less than the corresponding median X-ray positional uncertainty.

Owing to the factor of ≈2 increase in exposure/source counts from 2 Ms to 4 Ms, the areas of source positional error regions are expected to be reduced by ≈30% on average (see Section 4.2 of L10). We thus compared our positional uncertainties with the positional uncertainties for the 440 main-catalog sources that were previously detected in the L08 main catalog (see the description of Column 59 of the main catalog in Section 4.4). We find a median ratio of 0.82 between our and the L08 positional uncertainties[41] (corresponding to a median ratio of 0.67 between areas of our and the L08 positional error regions); such an improvement is in agreement with the above expectation. We also cross-matched the 462 L08 main-catalog sources with the 359 radio sources in the field using a matching radius of 2″, taking into account the systematic positional offsets between the optical catalogs and the VLA radio catalog (see Section 3.1). The median positional offset is 0.″40 between the L08 main-catalog sources and their radio counterparts for a total of 94 matches, as opposed to 0.″24 in our case. This significant improvement is not only because of the improved photon statistics, but also because we locked the astrometry of the combined X-ray images to the VLA radio sources rather than the WFI *R*-band sources that were adopted by L08.

4.3. Multiwavelength Identifications

We utilized the likelihood-ratio matching procedure presented in Section 2 of L10 to identify the optical/near-infrared/infrared/radio (ONIR) counterparts for the main-catalog X-ray sources. Briefly, the likelihood-ratio technique (e.g., Sutherland & Saunders 1992; Ciliegi et al. 2003; Brusa et al. 2005, 2007) searches for probable counterparts taking into account the positional accuracy of both the ONIR and *Chandra* X-ray sources and also the expected magnitude distribution of the counterparts. Compared to a simple matching method that searches for the nearest counterpart within a given radius, the likelihood-ratio method significantly reduces the false-match probability toward faint ONIR magnitudes (see, e.g., Section 2.4 of L10).

We used seven ONIR catalogs for identification purposes (see Table 1 of L10 for further details).

1. The ESO 2.2 m WFI *R*-band catalog (denoted as "WFI"; Giavalisco et al. 2004), with a 5σ limiting AB magnitude (Oke & Gunn 1983) of 27.3.
2. The GOODS-S *Hubble Space Telescope* (*HST*) version r2.0z *z*-band catalog (denoted as "GOODS-S"; Giavalisco et al. 2004), with a 5σ limiting AB magnitude of 28.2.
3. The GEMS *HST* *z*-band catalog (denoted as "GEMS"; Caldwell et al. 2008), with a 5σ limiting AB magnitude of 27.3.
4. The GOODS-S MUSIC catalog (denoted as "MUSIC"; Grazian et al. 2006; we used the *K*-selected sources in the V2 catalog that was presented in Santini et al. 2009) based on the Retzlaff et al. (2010) Very Large Telescope/ISAAC data, with a limiting *K*-band AB magnitude of 23.8 (at 90% completeness).
5. The MUSYC *K*-band catalog (denoted as "MUSYC"; Taylor et al. 2009), with a 5σ limiting AB magnitude of 22.4.
6. The SIMPLE *Spitzer*/IRAC 3.6 μm catalog (denoted as "SIMPLE"; Damen et al. 2011), with a 5σ limiting AB magnitude of 23.8.
7. The VLA 1.4 GHz radio catalog (denoted as "VLA"; Miller et al. 2008), with a 5σ limiting flux density of ≈40μJy.

As mentioned in Section 3.1, we find systematic positional offsets between the optical/near-infrared catalogs and the radio catalog and have chosen to shift all the optical and near-infrared/infrared source positions throughout this paper by 0.″175 in right ascension and −0.″284 in declination to be consistent with the radio astrometry.

We found that 716 (96.8%) of the 740 main-catalog sources have ONIR counterparts. For an X-ray source having multiple counterparts from the likelihood-ratio matching (108 such cases), we chose a primary counterpart from, in order of priority, the VLA, GOODS-S, GEMS, MUSIC, WFI, MUSYC, or SIMPLE catalog. This order is chosen based on several related factors: the positional accuracy, angular resolution (to minimize any blending effects), false-match probability, and catalog depth. Manual adjustments were made to a few sources based on visual inspection (e.g., we selected the optical position rather than the VLA radio position if the radio counterpart is clearly extended; see Section 2.3 of L10 for more details).

We used the Monte Carlo approach described in Broos et al. (2007, 2011) to estimate the false-match probability for each ONIR catalog. The main-catalog X-ray sources are considered to consist of two populations: an "associated population" for which true counterparts are expected in an ONIR catalog, and an "isolated population" for which no counterparts are expected (e.g., the true counterparts may be too faint or blended with other sources and thus not included) in an ONIR catalog. We estimated the false-match probability for the associated population by producing a mock ONIR counterpart for each X-ray source and running the likelihood-ratio matching procedure to find the counterpart recovery fraction. The offset between the mock counterpart and the X-ray source is selected randomly

[41] In L08, the X-ray positional uncertainties are quoted at the ≈85% confidence level. For straightforward comparison, we thus adopted the ≈68% confidence level positional uncertainties reported in Table 2 of L10 that were used in the L10 likelihood-ratio matching procedure (see Section 4.3 for more details).

Table 2
Overview of Columns in the Main *Chandra* Source Catalog

Column	Description
1	Source sequence number (i.e., XID)
2, 3	Right ascension and declination of the X-ray source
4	Minimum value of log P among the three standard bands (P is the AE-computed binomial no-source probability)
5	Logarithm of the minimum WAVDETECT false-positive probability detection threshold
6	≈68% confidence level X-ray positional uncertainty
7	Off-axis angle of the X-ray source
8–16	Aperture-corrected net (i.e., background-subtracted) source counts and the corresponding errors for the three standard bands
17	Flag of whether a source shows any evidence for spatial extent
18, 19	Right ascension and declination of the optical/near-infrared/infrared/radio (ONIR) counterpart
20	Offset between the X-ray source and ONIR counterpart
21	AB magnitude of the ONIR counterpart
22	Name of the ONIR catalog from which the primary counterpart has been taken
23–43	Right ascension, declination, and AB magnitude of the counterpart in seven ONIR catalogs
44–46	Spectroscopic redshift, redshift quality flag, and the reference for the redshift
47–57	Photometric-redshift information taken from sources in the literature
58	Preferred redshift adopted in this paper
59	Corresponding 2 Ms CDF-S source number from the main and supplementary *Chandra* catalogs presented in L08
60, 61	Right ascension and declination of the corresponding L08 source
62	Corresponding 250 ks E-CDF-S source number from the main and supplementary *Chandra* catalogs presented in L05
63, 64	Right ascension and declination of the corresponding L05 E-CDF-S source
65–67	Effective exposure times derived from the exposure maps for the three standard bands
68–70	Band ratio and the corresponding errors
71–73	Effective photon index with the corresponding errors
74–76	Observed-frame fluxes for the three standard bands
77	Absorption-corrected, rest-frame 0.5–8 keV luminosity
78	Estimate of likely source type
79	Notes on the source

based on the positional uncertainties, and the magnitude of the mock counterpart is drawn randomly from the expected magnitude distribution of the counterparts (derived previously in the likelihood-ratio matching procedure). The mock ONIR catalog is thus composed of the mock counterparts and the original ONIR catalog with source positions shifted and potential counterparts removed. To estimate the false-match probability for the isolated population, we shifted the X-ray source positions and recorrelated the shifted sources with the ONIR sources using likelihood-ratio matching. The above simulations were performed 100 times for each X-ray source population, and the results were used to solve for the final false-match probability for each ONIR catalog (see Broos et al. 2011 for details). The false-match probability for the associated population is generally smaller than that for the isolated population, and the final false-match probability for each ONIR catalog is <4%. The expected mean false-match probability for the main-catalog sources is ≈2.1%, derived by weighting the false-match probabilities of individual ONIR catalogs with the number of primary counterparts in each catalog. We note that the high identification rate, combined with the small false-match rate, provides independent evidence that the vast majority of our X-ray detections are robust.

For the 24 main-catalog sources that do not have highly significant multiwavelength counterparts, we visually inspected the X-ray images and found that the majority of them have apparent or strong X-ray signatures. Of these 24 sources, 19 were detected in the full band, with a median number of full-band counts of 49.8; 17 were detected in the soft band, with a median number of soft-band counts of 40.5; 9 were detected in the hard band, with a median number of hard-band counts of 58.7; and 17 were detected in at least two of the three standard bands. We also investigated the *Chandra* events for these 24 sources and concluded that they were not compromised by short-lived cosmic-ray afterglows. Of these 24 unidentified sources, 5 were previously detected in the L08 main catalog, 3 were previously detected in the L08 supplementary CDF-S plus E-CDF-S *Chandra* catalog, and 16 were only detected in the 4 Ms observations. As for the nature of these 24 unidentified sources, we refer readers to Section 4.1 of L10 and references therein for detailed discussion of the possibilities. For example, 5 of these 24 unidentified sources are probably related to off-nuclear X-ray sources associated with nearby galaxies (e.g., Hornschemeier et al. 2004; Lehmer et al. 2006; note that, in this paper, we did not attempt a thorough identification of off-nuclear X-ray sources).

4.4. Main-catalog Details

We summarize in Table 2 the columns (a total of 79) in the main *Chandra* X-ray source catalog; the main catalog itself is presented in Table 3. The details of the 79 columns are given below.

1. Column 1 gives the source sequence number (i.e., XID). We list sources in order of increasing right ascension.
2. Columns 2 and 3 give the right ascension and declination of the X-ray source, respectively. We determined source positions following the procedure detailed in Section 3.2. To avoid truncation error, we quote the positions to higher precision than in the International Astronomical Union registered names that begin with the acronym "CXO CDFS."
3. Columns 4 and 5 give the minimum value of log P (P is the AE-computed binomial no-source probability) among the three standard bands, and the logarithm of the minimum WAVDETECT false-positive probability detection threshold, respectively. More negative values of log P (Column 4) and

Table 3
Main *Chandra* Source Catalog

	X-ray Coordinates		Detection Probability				Counts					
No.	α_{2000}	δ_{2000}	log P	WAVDETECT	Pos Err	Off-axis	FB	FB Upp Err	FB Low Err	SB	SB Upp Err	SB Low Err
(1)	(2)	(3)	(4)	(5)	(6)	(7)	(8)	(9)	(10)	(11)	(12)	(13)
1...	03 31 35.79	−27 51 36.0	−99.0	−8	0.5	11.98	186.8	19.0	17.9	117.8	13.5	12.4
2...	03 31 40.12	−27 47 46.6	−30.9	−8	0.5	10.62	155.7	19.8	18.6	101.5	13.4	12.2
3...	03 31 41.01	−27 44 34.7	−15.6	−8	0.6	11.10	96.5	15.7	14.5	31.5	8.5	7.3
4...	03 31 43.25	−27 54 05.6	−6.5	−5	0.8	11.41	54.1	13.8	12.6	19.9	−1.0	−1.0
5...	03 31 43.42	−27 51 03.8	−5.9	−8	0.5	10.21	109.0	27.5	25.7	38.1	14.7	12.9

Notes. Units of right ascension are hours, minutes, and seconds, and units of declination are degrees, arcminutes, and arcseconds. The full table contains 79 columns of information for the 740 X-ray sources.

(This table is available in its entirety in a machine-readable form in the online journal. A portion is shown here for guidance regarding its form and content.)

false-positive probability threshold (Column 5) indicate a more significant source detection. We set log $P = -99.0$ for sources with $P = 0$. For the main-catalog sources, the median value of log P is −8.9 (note that $P < 0.004$, corresponding to log $P < -2.4$, is the condition for a source to be included in the main catalog). There are 493, 57, 69, and 121 sources with minimum WAVDETECT probabilities[38] of 10^{-8}, 10^{-7}, 10^{-6}, and 10^{-5}, respectively (see Figure 5).

4. Column 6 gives the ≈68% confidence level X-ray positional uncertainty in arcseconds computed using Equation (2), which is dependent on both off-axis angle and aperture-corrected net source counts. The ≈68% confidence-level X-ray positional uncertainty was used in the likelihood-ratio matching procedure (see Section 4.3). The positional uncertainty for the main-catalog sources ranges from 0.″10 to 1.″51, with a median value of 0.″42.

5. Column 7 gives the off-axis angle of the X-ray source in arcminutes, which is the angular separation between the X-ray source (coordinates given in Columns 2 and 3) and the CDF-S average aim point (given in Table 1). The off-axis angle for the main-catalog sources ranges from 0.′33 to 12.′36, with a median value of 5.′82. The maximum off-axis angle of 12.′36 is slightly larger than a half of the diagonal size of the ACIS-I field of view (11.′95), due to the fact that the CDF-S observations have varying aim points and roll angles, as shown in Table 1.

6. Columns 8–16 give the aperture-corrected net (i.e., background-subtracted) source counts and the corresponding 1σ upper and lower statistical errors (Gehrels 1986) for the three standard bands, respectively. The photometry was calculated by AE using the position given in Columns 2 and 3 for all bands and following the procedure described in Section 3.2, and was not corrected for vignetting or exposure-time variations. To be consistent with our source-detection criterion (i.e., $P < 0.004$), we considered a source to be "detected" for photometry purposes in a given band only if the AE-computed binomial no-source probability for that band is less than 0.004. For sources not detected in a given band, we calculated upper limits and placed −1.00 in the corresponding error columns. When the total number of counts within the polygonal extraction region of an undetected source was ⩽10, we computed the upper limit using the Bayesian method of Kraft et al. (1991) for a 99% confidence level; otherwise, we computed the upper limit at the 3σ level for Poisson statistics (Gehrels 1986).

7. Column 17 gives a flag indicating whether a source shows any evidence for spatial extent in basic testing. In Section 3.2, we ran WAVDETECT using nine wavelet scales up to 16 pixels, which potentially allows detection of sources that are extended on such scales. We utilized the following procedure to assess extent. We first derived a set of cumulative EEFs by extracting the PSF power within a series of circular apertures (centered at the source position) up to a 90% EEF radius from the merged PSF image. We then derived another set of cumulative EEFs by extracting source counts within a series of circular apertures (also centered at the source position) up to the same 90% EEF radius from the merged source image. Finally, we used a Kolmogorov–Smirnov (K-S) test suitable for two distributions to compute the probability ($\rho_{\rm K-S}$) that the two sets of cumulative EEFs are consistent with each other. Of the 740 main-catalog sources, 7 have $\rho_{\rm K-S} \leqslant 0.01$ (i.e., the merged PSF and source images are inconsistent with each other at or above a 99% confidence level) and have the value of this column set to 2; 24 have $0.01 < \rho_{\rm K-S} \leqslant 0.05$ and have the value of this column set to 1; all the remaining sources have the value of this column set to 0. A total of 31 main-catalog sources are flagged as 1 or 2 that corresponds to a ⩾95% confidence level, which is comparable to the expected number of false-positive determinations, i.e., $37 = 740 \times (1 - 95\%)$. These 31 sources are located across the entire CDF-S field and do not show the likely expected pattern of central clustering (since the PSF is sharpest near the field center), which might also indicate that many of these sources could be false positives. Moreover, we did not find any significant signature of extension for these 31 sources upon visual inspection. For the sources that truly have slight extents or are point sources sitting on top of highly extended sources, our AE-computed photometry should be reasonably accurate, as detailed in Section 3.2. We note that a few highly extended sources in the CDF-S (e.g., Giacconi et al. 2002; L05) cannot be identified here because these sources have larger extents than the maximum value of our adopted wavelet scales (i.e., 16 pixels); a full study of such extended sources is beyond the scope of this paper and will be presented in A. Finoguenov et al. (2011, in preparation).

8. Columns 18 and 19 give the right ascension and declination of the ONIR counterpart (see Section 4.3 for the

details of multiwavelength identifications). Sources without multiwavelength identifications have these right ascension and declination values set to "0 00 00.00" and "−00 00 00.0".

9. Column 20 gives the measured offset between the X-ray source and ONIR counterpart in arcseconds. Sources without multiwavelength identifications have a value set to −1.00.
10. Column 21 gives the AB magnitude of the ONIR counterpart, measured in the counterpart-detection band.[42] Sources without counterparts have a value set to −1.00.
11. Column 22 gives the name of the ONIR catalog (i.e., VLA, GOODS-S, GEMS, MUSIC, WFI, MUSYC, or SIMPLE) from which the primary counterpart has been taken. Sources without counterparts have this column set to "...."
12. Columns 23–43 give the right ascension, declination, and AB magnitude of the counterpart in the above seven ONIR catalogs that are used for identifications (i.e., WFI, GOODS-S, GEMS, MUSIC, MUSYC, SIMPLE, and VLA). We cross-matched the positions of primary ONIR counterparts (i.e., Columns 17 and 18) with the seven ONIR catalogs using likelihood-ratio matching. Sources without counterparts have corresponding right ascension and declination values set to "0 00 00.00" and "−00 00 00.0" and AB magnitudes set to −1.00. We find ≈75%, 61%, 72%, 55%, 70%, 88%, and 18% of the main-catalog X-ray sources have WFI, GOODS-S, GEMS, MUSIC, MUSYC, SIMPLE, and VLA counterparts,[43] respectively, with a false-match probability of <2% for each ONIR catalog (see Section 4.3 for details).
13. Columns 44–46 give the spectroscopic redshift ($z_{\rm spec}$), redshift quality flag, and the reference for the redshift. Spectroscopic redshifts were collected from Le Fèvre et al. (2004), Szokoly et al. (2004), Zheng et al. (2004), Mignoli et al. (2005), Ravikumar et al. (2007), Vanzella et al. (2008), Popesso et al. (2009), Treister et al. (2009),[44] Balestra et al. (2010), and Silverman et al. (2010) with the reference numbers of 1–10 in Column 46, respectively. We cross-matched the positions of primary ONIR counterparts (i.e., Columns 18 and 19) with the above catalogs of spectroscopic redshifts using a matching radius of 0.″5. Of the 716 main-catalog sources that have multiwavelength identifications, 419 (58.5%) have spectroscopic redshift measurements. Three hundred forty-three (81.9%) of these 419 spectroscopic redshifts are secure, i.e., they are measured at $\gtrsim$95% confidence levels with multiple secure spectral features (flagged as "Secure" in Column 45); 76 (18.1%) of these 419 spectroscopic redshifts are insecure (flagged as "Insecure" in Column 45). We estimated the false-match probability to be $\lesssim$1% in all cases. Sources without spectroscopic redshifts have these three columns set to −1.000, "None," and −1, respectively.
14. Columns 47–57 give the photometric-redshift ($z_{\rm phot}$) information taken from sources in the literature. Columns 47–50 give the photometric redshift, the corresponding 1σ lower and upper bounds,[45] and the alternative photometric redshift (set to −1.000 if not available) from L10. Columns 51–54 give the photometric redshift, the corresponding 1σ lower and upper bounds, and the corresponding quality flag Q_z (smaller values of Q_z indicate better quality; $0 < Q_z \lesssim 1$–3 indicates a reliable photometric-redshift estimate) from Cardamone et al. (2010). Columns 55–57 give the photometric redshift and the corresponding 1σ lower and upper bounds[45] from Rafferty et al. (2011). We chose the above photometric-redshift catalogs because they utilized extensive multiwavelength photometric data and produced accurate photometric redshifts. L10 derived high-quality photometric redshifts for the 462 L08 main-catalog X-ray sources with a treatment of photometry that included utilizing likelihood-matching, manual source deblending, and appropriate upper limits. Cardamone et al. (2010) employed new medium-band Subaru photometry and a PSF-matching technique to create a uniform photometric catalog and derived photometric redshifts for over 80,000 sources in the E-CDF-S; their photometric redshifts are of high quality, in particular for bright sources. Rafferty et al. (2011) derived photometric redshifts for over 100,000 sources in the E-CDF-S, using a compiled photometric catalog that probes fainter magnitudes than the Cardamone et al. (2010) catalog by including sources in the GOODS-S MUSIC catalog (Grazian et al. 2006; Santini et al. 2009); their photometric redshifts are accurate down to faint fluxes. We cross-matched the positions of primary ONIR counterparts (i.e., Columns 18 and 19) with the above photometric-redshift catalogs using a matching radius of 0.″5. Of the 716 main-catalog sources that have multiwavelength identifications, 668 (93.3%) have photometric-redshift estimates from at least one source (this number excludes sources identified as stars, given in Column 78, that have all these columns set to −1.000). We estimate the false-match probability to be $\lesssim$1% in all cases. Sources without photometric redshifts have all these columns set to −1.000. We show in Figure 8 the histograms of (a) $(z_{\rm phot} - z_{\rm spec})/(1 + z_{\rm spec})$ and (b) $z_{\rm phot}$ for the above three sources of photometric redshift. It seems clear that the photometric redshifts from each of these three sources have high quality[46] in terms of accuracy and outlier percentage (see Figure 8(a)) and cover a similar range of $z \approx 0$–5 (see Figure 8(b)). We refer readers to the cited references for the respective details of the photometric-redshift derivations, the advantages of the adopted methodologies, and the caveats when using these photometric redshifts.
15. Column 58 gives the preferred redshift adopted in this paper. We chose redshifts, in order of preference, as follows: (1) secure spectroscopic redshifts; (2) insecure spectroscopic redshifts that are in agreement with at least one of

[42] The AB magnitudes for the radio counterparts were converted from the radio flux densities, $m({\rm AB}) = -2.5\log(f_\nu) - 48.60$.

[43] Note that the GOODS-S and MUSIC catalogs cover ≈39% of the CDF-S while the other five catalogs cover the entire CDF-S (see Table 1 of L10 for more details); ≈70% of the main-catalog sources are in the GOODS-S/MUSIC area (see Figure 15(a)).

[44] We flagged the spectroscopic redshifts from Treister et al. (2009) as "Insecure" since Treister et al. (2009) did not provide redshift quality flags.

[45] The photometric-redshift errors derived with the Zurich Extragalactic Bayesian Redshift Analyzer (Feldmann et al. 2006) generally underestimate the real errors by factors of ≈3 and ≈6 for the spectroscopic and non-spectroscopic samples, respectively (see, e.g., Section 3.4 of L10). Therefore, multiplying the photometric-redshift errors presented here by these corresponding factors (i.e., ≈3 and ≈6 for the spectroscopic and non-spectroscopic samples, respectively) will roughly give realistic 1σ errors.

[46] In Figure 8(a), the photometric redshifts from both L10 and Rafferty et al. (2011) appear to have smaller outlier percentages than those from Cardamone et al. (2010) because the spectral energy distribution templates were optimized using the spectroscopic-redshift information before template fitting in both L10 and Rafferty et al. (2011). Blind-test results show that the actual outlier percentages from L10 and Rafferty et al. (2011) are comparable to those from Cardamone et al. (2010; see, e.g., Section 3.4 of L10 for the details of blind tests).

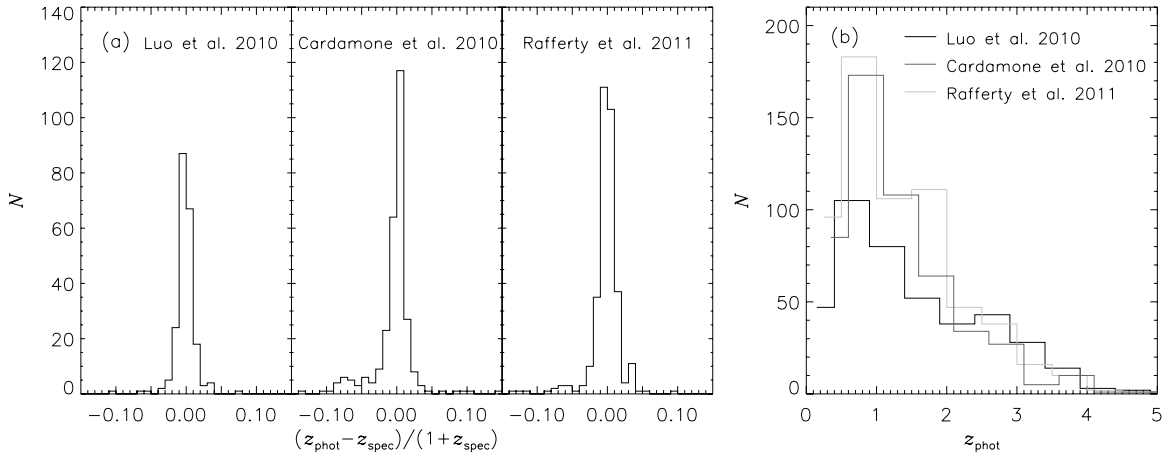

Figure 8. (a) Histogram of $(z_{phot} - z_{spec})/(1+z_{spec})$ for L10 (218 sources), Cardamone et al. (2010; 314 sources), and Rafferty et al. (2011; 339 sources). (b) Histogram of z_{phot} for L10 (black histogram; 417 sources), Cardamone et al. (2010; dark gray histogram; 508 sources), and Rafferty et al. (2011; light gray histogram; 611 sources). The histograms have been slightly shifted for clarity.

the L10, Cardamone et al. (2010), or Rafferty et al. (2011) photometric-redshift estimates (i.e., $|(z_{spec} - z_{phot})/(1 + z_{spec})| \leqslant 0.15$, where z_{spec}/z_{phot} is the spectroscopic/photometric redshift); (3) the L10 photometric redshifts; (4) the Cardamone et al. (2010) photometric redshifts; and (5) the Rafferty et al. (2011) photometric redshifts. Of the 716 main-catalog sources that have multiwavelength identifications, 673 (94.0%) have spectroscopic or photometric redshifts.

16. Column 59 gives the corresponding 2 Ms CDF-S source number from the main and supplementary *Chandra* catalogs presented in L08. We matched our X-ray source positions (i.e., Columns 2 and 3) to L08 source positions (corrected for the systematic positional shifts described in Section 3.1) using a 2.″5 matching radius for sources with off-axis angle $\theta < 6'$ and a 4.″0 matching radius for sources with $\theta \geqslant 6'$. The mismatch probability is ≈1% using this approach. For the 740 main-catalog sources, we find
    (a) Four hundred forty have matches to the 462 L08 main-catalog sources (the value of Column 59 is that from Column 1 of Table 2 in L08; see Section 4.5 for more details).
    (b) Forty-one have matches to the 86 L08 supplementary CDF-S plus E-CDF-S *Chandra* catalog sources (the value of Column 59 is that from Column 1 of Table 5 in L08 with a prefix of "SP1_," e.g., SP1_1).
    (c) Twenty-two have matches to the 30 L08 supplementary optically bright *Chandra* catalog sources (the value of Column 59 is that from Column 1 of Table 6 in L08 with a prefix of "SP2_," e.g., SP2_1).
    (d) Six were outside of the 2 Ms CDF-S footprint of L08 (the value of Column 59 is set to −1); the detection of these sources is simply due to the new sky coverage (rather than the improved sensitivity) of the 4 Ms CDF-S.
    (e) Two hundred thirty-one have no match in any of the L08 main and supplementary *Chandra* catalogs; these sources were inside the 2 Ms CDF-S footprint but are only detected now due to the improved sensitivity of the 4 Ms observations (the value of Column 59 is set to 0).

    In summary, of the 740 main-catalog sources, 503 were detected previously in the 2 Ms CDF-S observations (the value of Column 59 is greater than 0) and 237 were detected only in the 4 Ms observations (the value of Column 59 is either −1 or 0). Compared to the L08 main catalog, there are 300 (i.e., 740 − 440 = 300) new main-catalog sources (see Section 4.7 for more details of these 300 sources).
17. Columns 60 and 61 give the right ascension and declination of the corresponding L08 source (corrected for the systematic positional shifts described in Section 3.1) indicated in Column 59. Sources without an L08 match have right ascension and declination values set to "0 00 00.00" and "−00 00 00.0".
18. Column 62 gives the corresponding 250 ks E-CDF-S source number from the main and supplementary *Chandra* catalogs presented in L05. We adopted the same matching approach between X-ray catalogs as used for Column 59, again with the E-CDF-S source positions corrected for the systematic positional shifts described in Section 3.1. For the 740 main-catalog sources, we find that (1) 239 have matches in the E-CDF-S main *Chandra* catalog (the value of Column 62 is that from Column 1 of Table 2 in L05); (2) 5 have matches in the E-CDF-S supplementary optically bright *Chandra* catalog (the value of Column 62 is that from Column 1 of Table 6 in L05 with a prefix of "SP_," e.g., SP_1); and (3) 496 have no match in either of the E-CDF-S main or supplementary *Chandra* catalogs (the value of Column 62 is set to 0).
19. Columns 63 and 64 give the right ascension and declination of the corresponding L05 E-CDF-S source (corrected for the systematic positional shifts described in Section 3.1) indicated in Column 62. Sources without an E-CDF-S match have right ascension and declination values set to "0 00 00.00" and "−00 00 00.0".
20. Columns 65–67 give the effective exposure times derived from the exposure maps (detailed in Section 3.1) for the full, soft, and hard bands. Dividing the counts in Columns 8–16 by the corresponding effective exposure times will provide effective count rates that have been corrected for vignetting, quantum-efficiency degradation, and exposure-time variations.
21. Columns 68–70 give the band ratio and the corresponding upper and lower errors, respectively. We defined the band ratio as the ratio of counts between the hard and soft bands, correcting for differential vignetting between the hard

and soft bands using the appropriate exposure maps. We followed the numerical error-propagation method described in Section 1.7.3 of Lyons (1991) to compute band-ratio errors. This method avoids the failure of the standard approximate variance formula when the number of counts is small and the error distribution is non-Gaussian (e.g., see Section 2.4.5 of Eadie et al. 1971). We calculated upper limits for sources detected in the soft band but not the hard band and lower limits for sources detected in the hard band but not the soft band. For these sources, we set the upper and lower errors to the computed band ratio. We set band ratios and corresponding errors to −1.00 for sources detected only in the full band.

22. Columns 71–73 give the effective photon index (Γ) with the corresponding upper and lower errors, respectively, for a power-law model with the Galactic column density given in Section 1. We calculated the effective photon index based on the band ratio in Column 68, using a conversion between the effective photon index and the band ratio. We derived this conversion using the band ratios and photon indices calculated by the AE-automated XSPEC-fitting procedure for relatively bright X-ray sources (with full-band counts greater than 200; this ensures reliable XSPEC-fitting results). This approach takes into account the multi-epoch *Chandra* calibration information and thus has an advantage over methods using only single-epoch calibration information such as the CXC's Portable, Interactive, Multi-Mission Simulator method used by L08. We calculated upper limits for sources detected in the hard band but not the soft band and lower limits for sources detected in the soft band but not the hard band. For these sources, we set the upper and lower errors to the computed effective photon index. For low-count sources, we are unable to determine the effective photon index reliably; we therefore assumed $\Gamma = 1.4$, which is a representative value for faint sources that should yield reasonable fluxes, and set the corresponding upper and lower errors to 0.00. We defined sources with a low number of counts as being (1) detected in the soft band with <30 counts and not detected in the hard band, (2) detected in the hard band with <15 counts and not detected in the soft band, (3) detected in both the soft and hard bands, but with <15 counts in each, or (4) detected only in the full band.
23. Columns 74–76 give observed-frame fluxes in units of erg cm^{-2} s^{-1} in the full, soft, and hard bands. We computed fluxes using the counts in Columns 8–16, the appropriate exposure maps (Columns 65–67), and the effective power-law photon indices given in Column 71. We did not correct fluxes for absorptions by Galactic material or material intrinsic to the source. Negative flux values indicate upper limits. We note that, due to the Eddington bias, sources with low net counts (given in Columns 8–16) could have true fluxes lower than those computed here (see, e.g., Vikhlinin et al. 1995; Georgakakis et al. 2008). We do not attempt to correct for the Eddington bias, since we aim to provide only observed fluxes here. Determining more accurate fluxes for these sources would require (1) using a number-count distribution prior to estimate the flux probabilities for sources near the sensitivity limit and/or (2) directly fitting the X-ray spectra for each observation; these analyses are beyond the scope of this paper.
24. Column 77 gives a basic estimate of the absorption-corrected, rest-frame 0.5–8 keV luminosity ($L_{0.5-8\ \mathrm{keV}}$) in units of erg s^{-1}. We calculated $L_{0.5-8\ \mathrm{keV}}$ using the procedure detailed in Section 3.4 of Xue et al. (2010). Briefly, this procedure models the X-ray emission using a power law with both intrinsic and Galactic absorption (i.e., $zpow \times wabs \times zwabs$ in XSPEC) to find the intrinsic column density that reproduces the observed band ratio (given in Column 68), assuming a typical power-law photon index of $\Gamma_{\mathrm{int}} = 1.8$ for intrinsic AGN spectra. It then corrects for both Galactic and intrinsic absorption to obtain the absorption-corrected flux ($f_{0.5-8\ \mathrm{keV,int}}$; as opposed to the observed flux given in Column 74), and follows the equation $L_{0.5-8\ \mathrm{keV}} = 4\pi d_L^2 f_{0.5-8\ \mathrm{keV,int}}(1+z)^{\Gamma_{\mathrm{int}}-2}$ to derive $L_{0.5-8\ \mathrm{keV}}$ (where d_L is the luminosity distance and z is the adopted redshift given in Column 58). In this procedure, we set the observed band ratio to a value that corresponds to $\Gamma = 1.4$ for sources detected only in the full band; for sources having upper or lower limits on the band ratio, we adopted their upper or lower limits for this calculation. Basic luminosity estimates derived in this manner are generally found to agree with those from direct spectral fitting to within a factor of ≈30%;[47] the direct spectral-fitting approach should produce more reliable estimates, but is beyond the scope of this paper. Sources without redshift estimates have this column set to −1.000; negative luminosity values other than −1.000 indicate upper limits.
25. Column 78 gives a basic estimate of likely source type. We categorized the X-ray sources into three basic types: "AGN," "Galaxy," and "Star." We utilized four criteria that are based on distinct AGN physical properties and one criterion that is based on optical spectroscopic information to identify AGN candidates, which must satisfy at least one of these five criteria. We briefly describe these criteria below.
    (a) A source with an intrinsic X-ray luminosity (given in Column 77) of $L_{0.5-8\ \mathrm{keV}} \geqslant 3 \times 10^{42}$ erg s^{-1} will be identified as a luminous AGN.
    (b) A source with an effective photon index (given in Column 71) of $\Gamma \leqslant 1.0$ will be identified as an obscured AGN.
    (c) A source with an X-ray-to-optical flux ratio of $\log(f_X/f_R) > -1$ (where $f_X = f_{0.5-8\ \mathrm{keV}}$, $f_{0.5-2\ \mathrm{keV}}$, or $f_{2-8\ \mathrm{keV}}$) will be identified as an AGN.
    (d) A source with excess (i.e., a factor of ⩾3) X-ray emission over the level expected from pure star formation will be identified as an AGN, i.e., with $L_{0.5-8\ \mathrm{keV}} \gtrsim 3 \times (8.9 \times 10^{17} L_R)$, where L_R is the rest-frame 1.4 GHz monochromatic luminosity in units of W Hz^{-1} and $8.9 \times 10^{17} L_R$ is the expected X-ray emission level that originates from starburst galaxies (see Alexander et al. 2005 for the details of this criterion).
    (e) A source with optical spectroscopic AGN features such as broad emission lines and/or high-excitation emission lines will be identified as an AGN; we cross matched the sources (using the ONIR counterpart positions given in Columns 18 and 19) with the spectroscopically identified AGNs in Szokoly et al.

[47] We caution that our basic $L_{0.5-8\ \mathrm{keV}}$ estimates could be subject to larger uncertainties for heavily obscured AGNs. This is not only due to the increasing difficulty in determining the intrinsic column density from the observed band ratio, but also due to the fact that other components (e.g., reflection and scattering) become stronger in such heavily obscured sources.

(2004), Mignoli et al. (2005), and Silverman et al. (2010), using a matching radius of 0.″5.

We note that the above five criteria are effective but not complete in identifying AGNs and refer readers to, e.g., Bauer et al. (2004), Alexander et al. (2005), Lehmer et al. (2008), and Xue et al. (2010) for discussions and caveats (e.g., low-luminosity and/or highly obscured AGNs may still not be identified through the criteria presented here). We also identified likely stars by cross-matching the sources (using the ONIR counterpart positions given in Columns 18 and 19) with (1) the spectroscopically identified stars in Szokoly et al. (2004), Mignoli et al. (2005), and Silverman et al. (2010); (2) the likely stars with stellarity indices greater than 0.7 in the GEMS *HST* catalog (Caldwell et al. 2008); and (3) the likely stars with best-fit stellar templates in the MUSYC photometric-redshift catalog (Cardamone et al. 2010), using a matching radius of 0.″5. We inspected each of the sources identified as stars in the *HST* images and retrieved sources that appear to be galaxies (i.e., set our classification to galaxy). The sources that were not identified as AGNs or stars are classified as "galaxies." Of the 740 main-catalog sources, 568 (76.8%), 162 (21.9%), and 10 (1.3%) are identified as AGNs, galaxies, and stars, respectively. Of the 568 AGNs in the main catalog, 65.1%, 40.3%, 91.7%, 14.8%, and 1.1% satisfy the criteria (a), (b), (c), (d), and (e), respectively.

26. Column 79 gives notes on the sources. We annotated sources at the field edge that lie partially outside of the survey area with "E" (one source only) and sources in close doubles or triples with "C" (a total of 35 sources; these 35 sources have overlapping polygonal extraction regions that correspond to ≈40%–75% EEFs; see Section 3.2). Sources not annotated have this column set to "...".

4.5. Comparison with 2 Ms CDF-S Main-catalog Sources

We summarize in Table 4 the source detections in the three standard bands. In total 740 sources are detected, with 634, 650, and 403 detected in the full, soft, and hard band, respectively. As stated earlier in Section 4.4 (see the description of Column 59), 503 of the main-catalog sources were detected in the L08 main or supplementary catalogs, among which 440 were detected in the L08 main catalog. For these 440 common sources, we find general agreement between the derived X-ray photometry presented here and in L08. For instance, the median ratio between our full-band count rates and the L08 full-band count rates for the 387 full-band detected sources (among these 440 common sources) is 1.03, with an interquartile range of 0.91–1.14. The ≈3% increase in the full-band count rates is mainly caused by a few updates to the ancillary response file (ARF) and contamination model in the CALDB data[48] since the production of the L08 catalogs. The detailed differences (e.g., scattering) in the derived X-ray photometry are mainly due to source variability and/or the above CALDB updates (e.g., sources with different X-ray spectral shapes are affected differently by these CALDB updates). The approximately doubled exposure improves the source positions and spectral constraints significantly. Hence, the 4 Ms CDF-S catalogs presented here supersede those in L08.

[48] For example, there was a recalibration of the ACIS-I ARF in CALDB 4.1.1 (released in 2009 January), yielding a flat ≈9% reduction in the effective area below 2 keV and a ≈0%–8% reduction between 2 and 5 keV (see http://cxc.harvard.edu/ciao/why/caldb4.1.1_hrma.html).

Table 4
Summary of *Chandra* Source Detections

Band (keV)	Number of Sources	Detected Counts Per Source			
		Maximum	Minimum	Median	Mean
Full (0.5–8.0)	634	35657.0	11.4	101.4	497.4
Soft (0.5–2.0)	650	25470.7	6.0	45.1	293.8
Hard (2–8)	403	10219.3	10.7	99.9	302.8

Twenty-two (i.e., 462−440 = 22) of the 462 sources detected in the L08 main catalog are not included in our main catalog, among which 3 are included in our supplementary catalog (see Section 5). Thus, there are a total of 19 "missing" L08 main-catalog sources not included in the 4 Ms main or supplementary catalogs. Among these 19 missing sources, there are two cases where a source was previously listed as being in a close pair but is now removed due to no apparent signature of a close pair in the 4 Ms images. Of the remaining 17 sources, 12, 3, and 2 have a logarithm of the minimum WAVDETECT false-positive probability detection threshold of −6, −7, and −8 in the L08 main catalog, respectively. Among these 17 sources, 9 have no multiwavelength counterparts and have no emission clearly distinct from the background in the 4 Ms images, which indicates that most of these 9 sources are likely false detections.[49] For the other eight sources that have relatively faint multiwavelength counterparts, they also have no apparent X-ray signatures in the 4 Ms images although a few of them have full-band counts of $\gtrsim$20–30 in the L08 catalog; these eight sources are likely real X-ray sources, but they are not detected in the 4 Ms images probably due to source variability and/or background fluctuations, as the second 2 Ms exposure was taken ≈2.5 years after the completion of the first 2 Ms exposure. Indeed, all of these eight sources were variable (at $\geqslant$99.7% confidence levels based on K-S tests) and became fainter (i.e., having a factor of $\gtrsim$2 smaller count rates) during the second 2 Ms of observations; consequently, the addition of background counts diluted their signals from the first 2 Ms of observations.[50] We note that source variability is not uncommon among the CDF sources: over short timescales (days to weeks) a ≈35% median flux variability for the sources in the first 2 Ms data set has been observed; over long timescales (years) source fluxes could vary by up to a factor of ≈5–10 in a few extreme cases (Paolillo et al. 2004; M. Paolillo et al. 2011, in preparation).

We summarize in Table 5 the number of sources detected in one band but not another. There are 21, 101, and 5 sources detected only in the full, soft, and hard band, respectively, as opposed to 31, 56, and 3 sources detected only in the full, soft, and hard band in the L08 main catalog.

4.6. Properties of Main-catalog Sources

In Figure 9, we show the distributions of detected counts in the three standard bands for the main-catalog sources. The median number of counts is ≈101, 45, and 100 for the full, soft, and hard band, respectively. There are 319 sources with >100 full-band counts, for which basic spectral analyses are possible; there are 202, 101, and 60 sources with >200, 500, 1000 full-band counts, respectively.

[49] We note that L08 estimated the number of false detections in their main catalog to be ≈18, which is a conservative estimate; the real number of false detections is likely ≈2–3 times smaller, i.e., ≈6–9 (see Section 3.2 of L08).

[50] Of these eight sources, only three satisfy the $P < 0.004$ criterion during the first 2 Ms exposure, while none satisfies the $P < 0.004$ criterion during the second 2 Ms exposure.

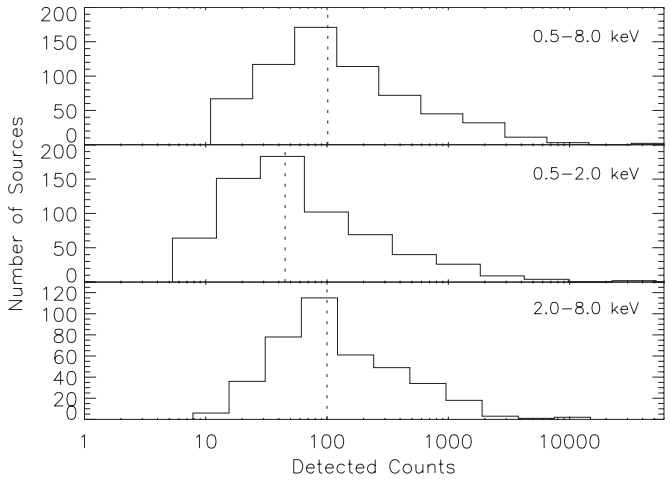

Figure 9. Histograms of detected source counts for the main-catalog sources in the full (top), soft (middle), and hard (bottom) bands. Sources with upper limits have not been included in the plots. The vertical dotted lines indicate median numbers of counts in each band (see Table 4).

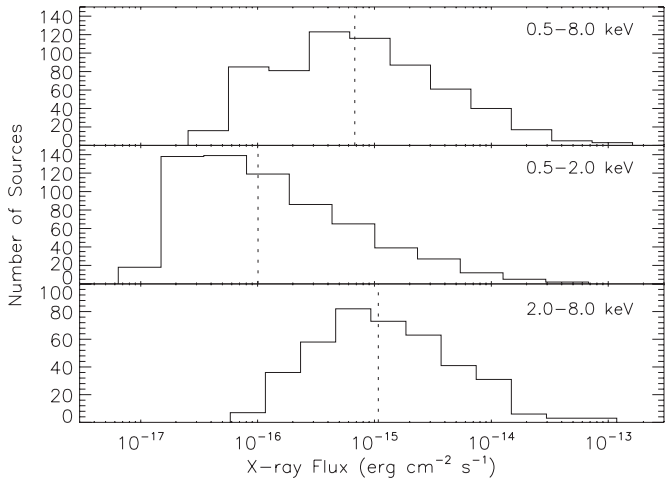

Figure 10. Histograms of X-ray fluxes for the main-catalog sources in the full (top), soft (middle), and hard (bottom) bands. Sources with upper limits have not been included in the plots. The vertical dotted lines indicate the median fluxes of 6.8×10^{-16}, 1.0×10^{-16}, and 1.1×10^{-15} erg cm^{-2} s^{-1} for the full, soft, and hard bands, respectively.

Table 5
Sources Detected in One Band but Not Another

Detection Band	Nondetection Energy Band		
(keV)	Full	Soft	Hard
Full (0.5–8.0)	...	85	236
Soft (0.5–2.0)	101	...	316
Hard (2–8)	5	69	...

Note. For example, there were 85 sources detected in the full band but not in the soft band.

In Figure 10, we show the distributions of X-ray flux in the three standard bands for the main-catalog sources. The X-ray fluxes span roughly four orders of magnitude, with a median value of 6.8×10^{-16}, 1.0×10^{-16}, and 1.1×10^{-15} erg cm^{-2} s^{-1} for the full, soft, and hard band, respectively.

We show in Figure 11 the distribution of the AE-computed no-source probability P (given in Column 4) for the main-catalog sources; sources without multiwavelength counterparts (given in Columns 18 and 19) are highlighted by shaded areas. It is clear

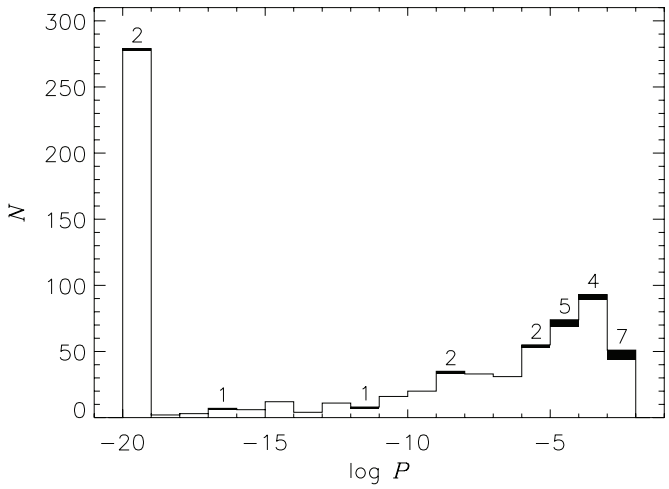

Figure 11. Histogram of the AE-computed binomial no-source probability, P, for the main-catalog sources. For the purpose of illustration, we set the values of $P < 10^{-20}$ to $P = 10^{-20}$ in this plot. The shaded areas indicate sources that have no multiwavelength counterparts, with the numbers of these unidentified sources listed above the corresponding shaded areas.

that the majority of the main-catalog sources have low no-source probabilities (i.e., with $\log P \leqslant -6$). We find that 1.3% of the $\log P \leqslant -6$ sources have no multiwavelength counterparts, as opposed to the 6.6% of $\log P > -6$ sources that lack multiwavelength counterparts. Combined with the small false-match rate (see Section 4.3), the above observations suggest that an X-ray source having a secure multiwavelength counterpart is an effective indicator of it being real.

We show in Figures 12–14 "postage-stamp" images from the WFI R-band, the GOODS-S/GEMS *HST* z-band, and the SIMPLE IRAC 3.6 μm band with adaptively smoothed full-band X-ray contours overlaid for the main-catalog sources, respectively. The size of X-ray sources in these images spans a wide range largely due to PSF broadening with off-axis angle.

4.7. Properties of the 300 New Main-catalog Sources

In this section, we examine the properties of the 300 main-catalog sources that were not detected in the L08 main catalog (hereafter new sources), putting emphasis on the comparison with the sources previously detected in the L08 main catalog (hereafter old sources; a total of $740 - 300 = 440$ sources).

Figure 15(a) shows the positions of the new sources (shown as filled symbols) and the old sources (shown as open symbols), with source types (given in Column 78) being color-coded (red for AGNs, black for galaxies, and blue for stars, respectively). Different symbol sizes represent different AE binomial no-source probabilities (see Column 4 of Table 3), with larger sizes indicating lower no-source probabilities (i.e., higher source-detection significances). In the GOODS-S region, there are 512 main-catalog sources, with 221 being new; in the Cosmic Assembly Near-IR Deep Extragalactic Legacy Survey (CANDELS) region, there are 258 main-catalog sources, with 123 being new; and in the UDF region, there are 45 main-catalog sources, with 20 being new. The source densities of both new and old sources decline toward large off-axis angles as the sensitivity decreases (see Section 7.2); such a trend appears more apparent among new sources than among old sources, e.g., 22.0% of new sources and while only 14.8% of old sources have $\theta < 3'$, and 62.0% of new sources and while only 46.1% of old sources have $\theta < 6'$, respectively. Figure 15(c) presents the observed source

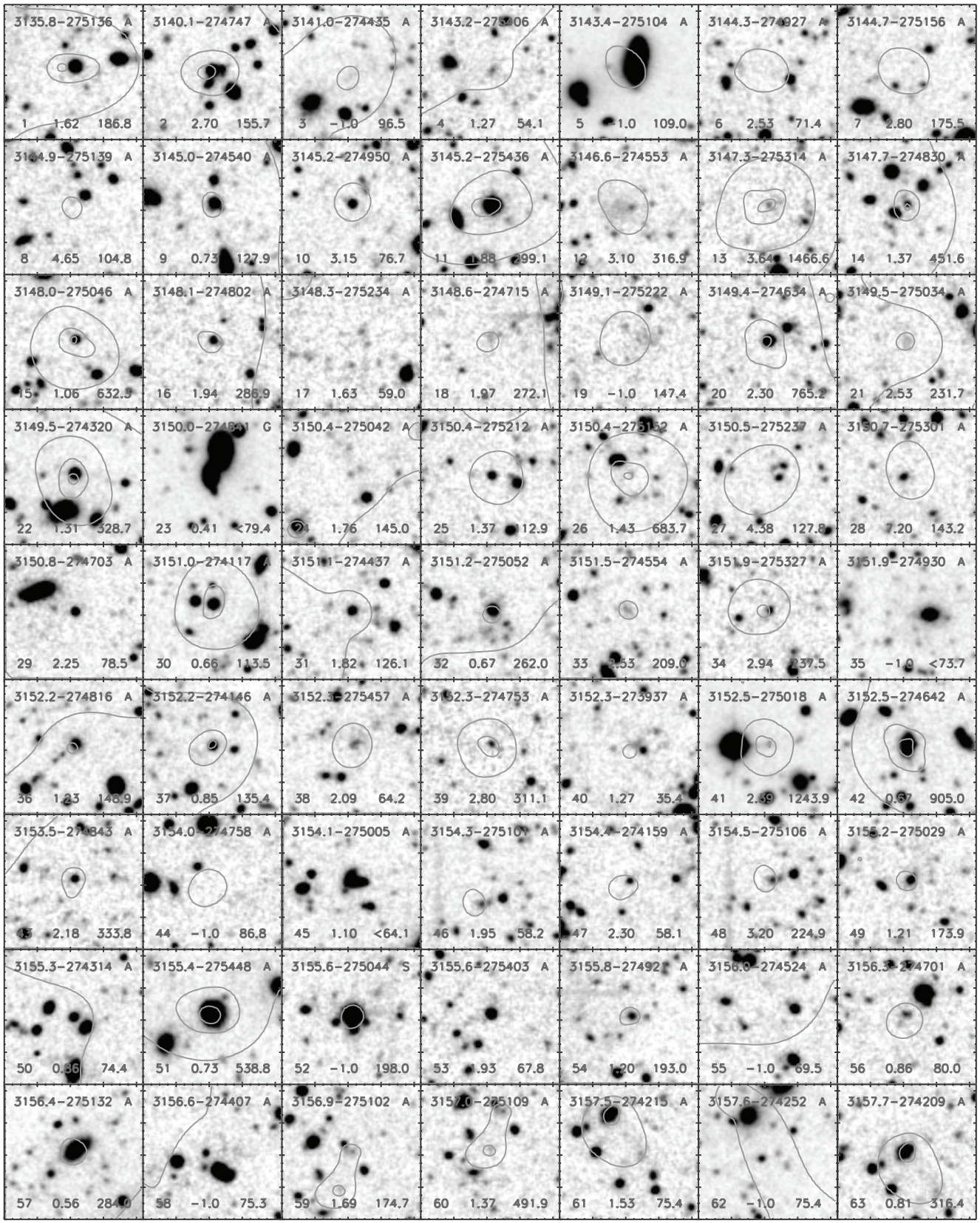

Figure 12. Typical postage-stamp images from the WFI *R* band for the main-catalog sources with full-band adaptively smoothed X-ray contours overlaid. The contours have a logarithmic scale and range from ≈0.003% to 30% of the maximum pixel value. The labels at the top of each image give the source name (for right ascension, the hours "03" have been omitted for succinctness) derived from the source coordinates and the source type ("A" denotes "AGN"; "G" denotes "Galaxy"; and "S" denotes "Star"). The numbers at the bottom of each image indicate the source number, the adopted redshift, and the full-band counts or upper limit (with a "<" sign). There are several cases where no X-ray contours are present, either because these sources were not detected in the full band or their full-band counts are low resulting in their observable emission in the adaptively smoothed images being suppressed by CSMOOTH. Each image is 25″ × 25″, with the source of interest located at the center. The cutouts of all the main-catalog sources are available in the online version of the journal.

(An extended version of this figure is available in the online journal.)

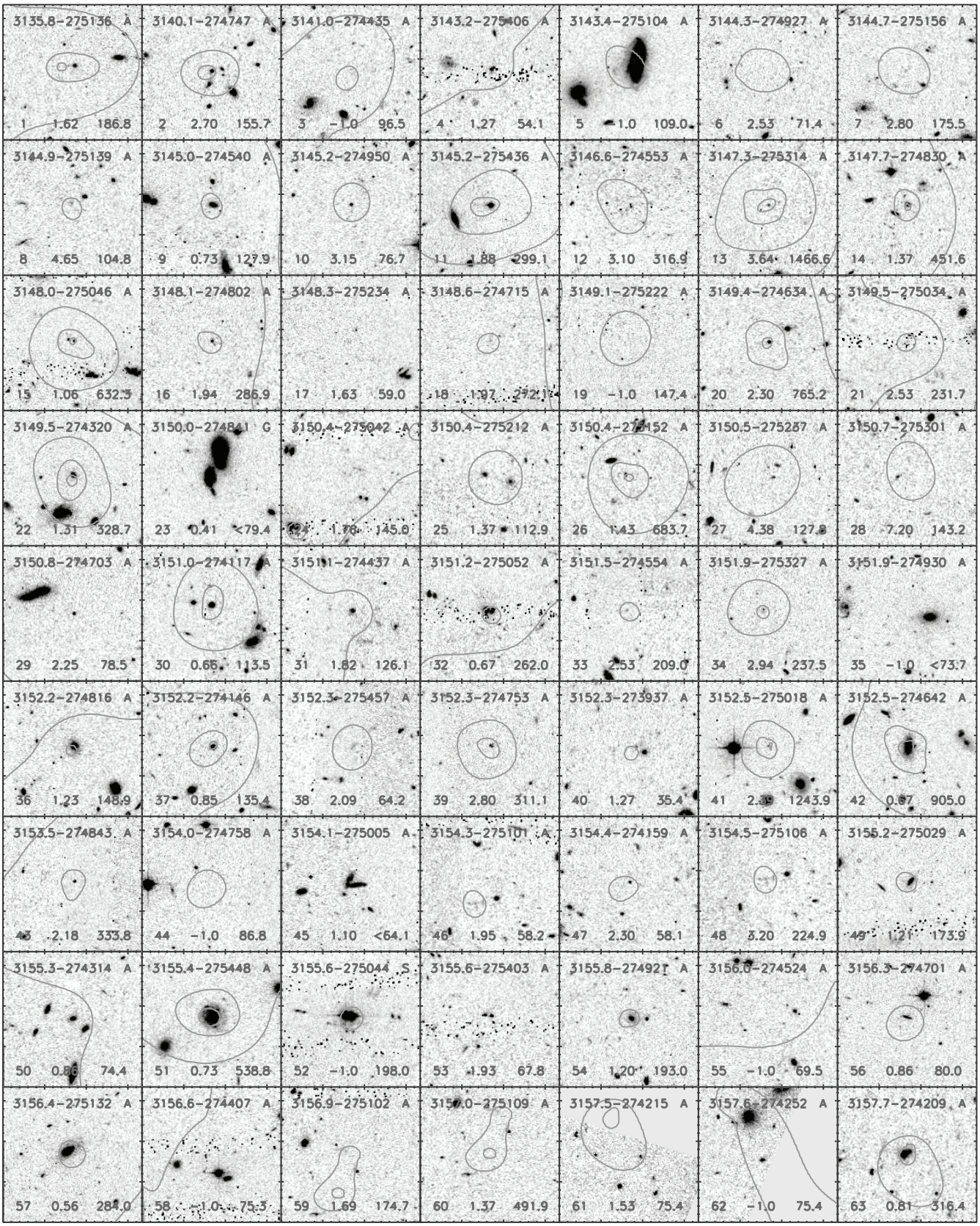

Figure 13. Same as Figure 12, but for the GOODS-S/GEMS *HST z* band. The cutouts of all the main-catalog sources are available in the online version of the journal. (An extended version of this figure is available in the online journal.)

density as a function of off-axis angle for all the main-catalog sources. Overall, AGNs have larger observed source densities than galaxies. However, since the slope of the observed galaxy number counts at faint fluxes is steeper than that of the observed

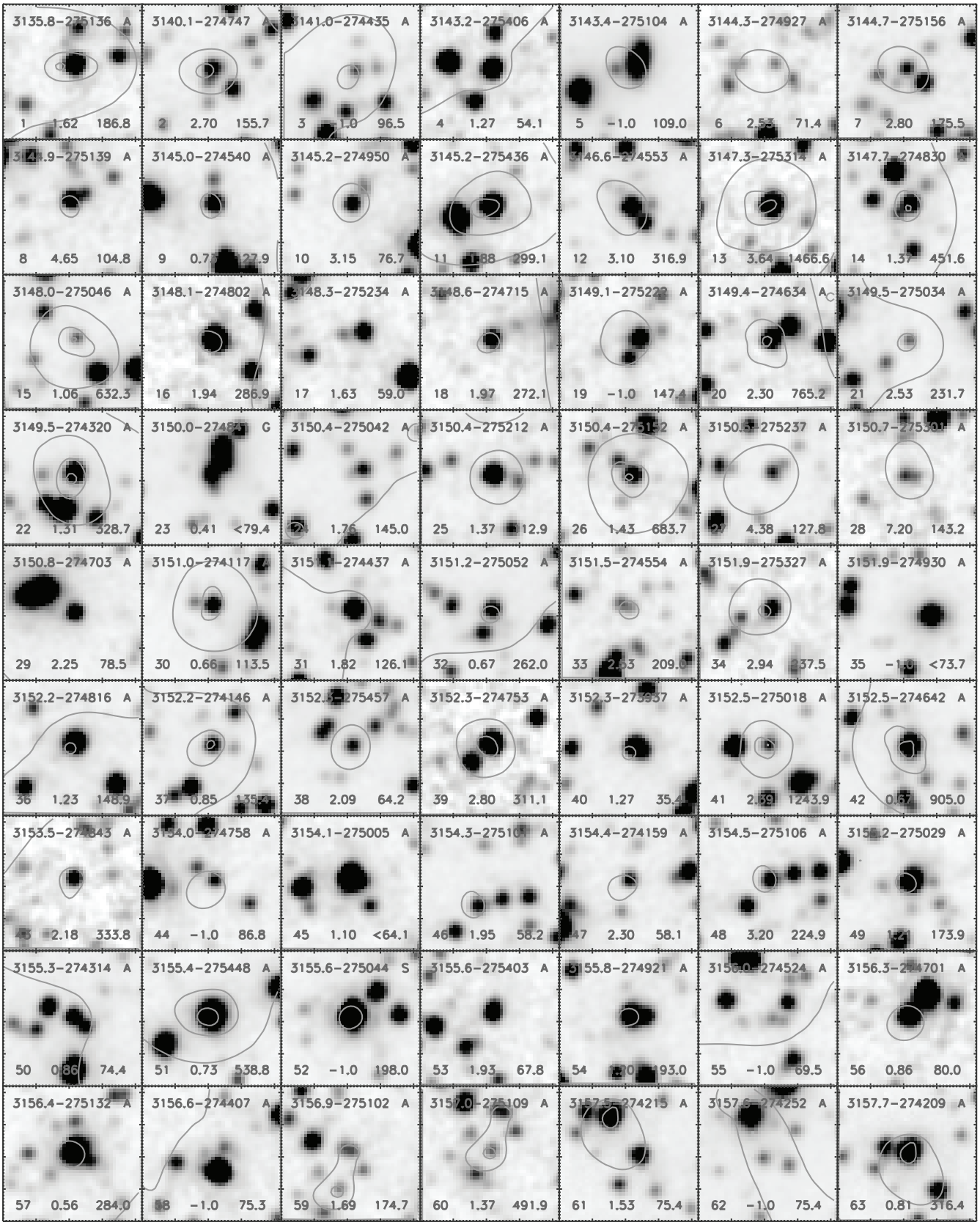

Figure 14. Same as Figure 12, but for the SIMPLE IRAC 3.6 μm band. The cutouts of all the main-catalog sources are available in the online version of the journal. (An extended version of this figure is available in the online journal.)

AGN number counts (e.g., Bauer et al. 2004), the galaxy source density approaches the AGN source density toward smaller off-axis angles (i.e., toward lower flux levels). This can also be seen in Figure 15(d) that plots the observed source density versus

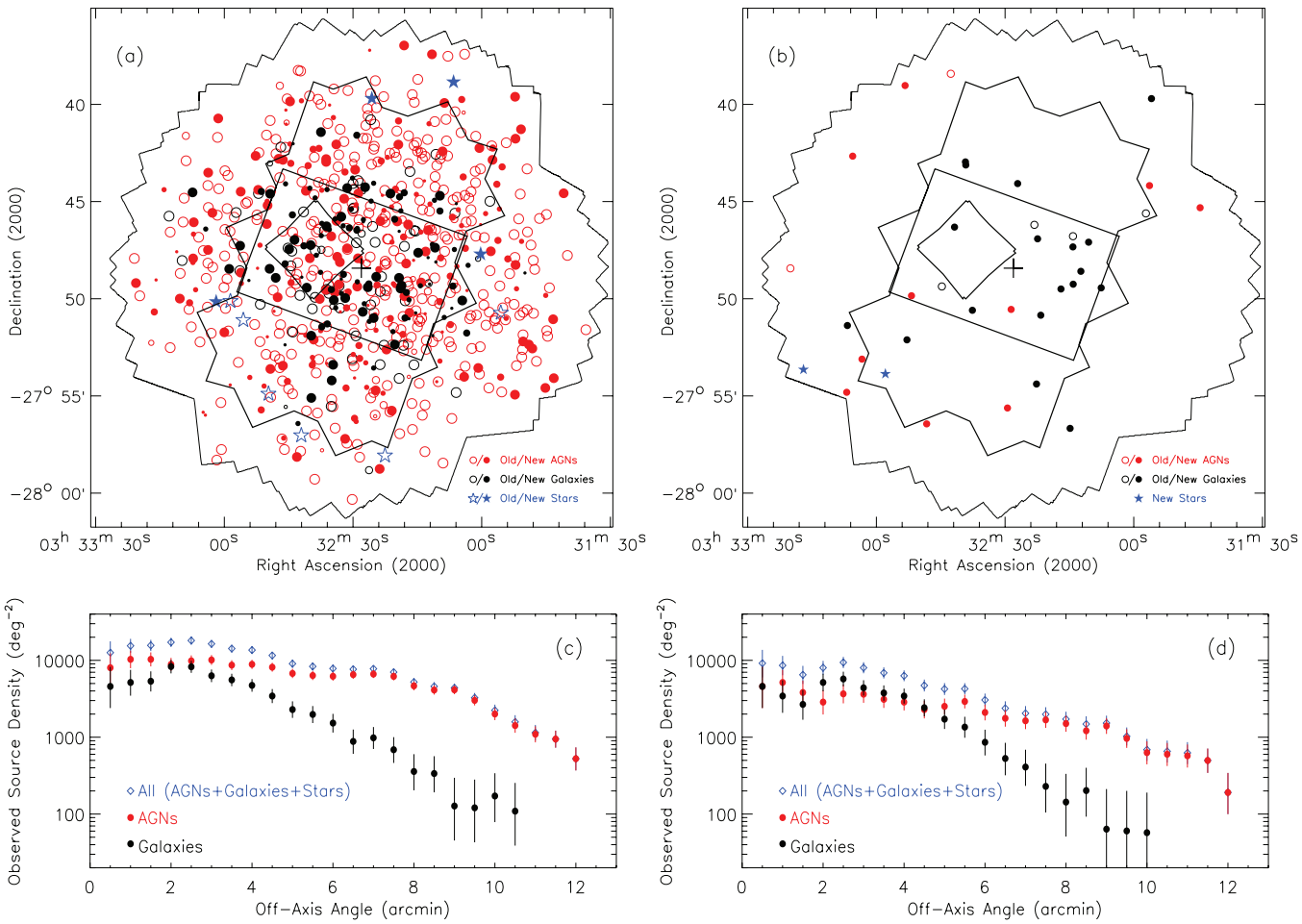

Figure 15. Top: source spatial distributions for (a) the main catalog and (b) the supplementary optically bright catalog. Sources that are considered as AGNs, galaxies, and stars (given in Column 78) are colored red, black, and blue, respectively. Open circles indicate AGNs/galaxies that were previously detected in (a) the L08 main catalog or (b) the L08 main or supplementary optically bright catalog; open stars in (a) indicate stars that were previously detected in the L08 main catalog; filled circles and stars indicate new AGNs/galaxies and stars, respectively. The regions and the plus sign are the same as those in Figure 1. In panel (a), the sizes of the circles and stars indicate the AE binomial no-source probabilities, with larger sizes indicating lower no-source probabilities: as the size becomes smaller, the AE binomial no-source probability P moves from $\log P \leqslant -5$, $-5 < \log P \leqslant -4$, $-4 < \log P \leqslant -3$ to $\log P > -3$. In panel (b), all sources have $\log P > -3$ and are plotted as circles/stars of the same size. Bottom: observed source density for different source types as a function of off-axis angle for (c) all the main-catalog sources and (d) the new main-catalog sources, as computed in bins of $\Delta\theta = 1'$. 1σ errors are calculated using Poisson statistics.

(A color version of this figure is available in the online journal.)

off-axis angle for new sources; within $\theta = 3'$, the new galaxies already outnumber the new AGNs (36 versus 30). Near the center of the 4 Ms CDF-S (within $\theta = 3'$), as shown in Figure 15(c), the overall observed AGN and galaxy source densities have reached 9800^{+1300}_{-1100} deg^{-2} and 6900^{+1100}_{-900} deg^{-2}, respectively. We note that detailed analyses of the overall source densities for different source types, which consider effects such as the Eddington bias and incompleteness, are beyond the scope of this work.

We show in Figure 16 plots of (a) observed-frame full-band flux (given in Column 74) versus redshift (given in Column 58), (b) absorption-corrected, rest-frame 0.5–8 keV luminosity (given in Column 77) versus redshift, and (c) band ratio (given in Column 68) versus absorption-corrected, rest-frame 0.5–8 keV luminosity, for new sources (shown as filled circles) and old sources (shown as open circles), respectively. Compared to old sources, new sources typically have smaller full-band fluxes and 0.5–8 keV luminosities (see their clustering at the faint-flux end in Figure 16(a) and at the low-luminosity end in Figure 16(b)), which is expected since the 4 Ms CDF-S has fainter flux limits than the 2 Ms CDF-S. The existence of a small number of new sources at the high-flux/luminosity end leads to the full range of flux/luminosity for new sources being similar to that for old sources; these bright/luminous sources are typically located at relatively large off-axis angles. As shown in Figure 16(a), there is no apparent correlation between full-band flux and redshift for either new or old sources, and the 4 Ms CDF-S is detecting an appreciable number of the faintest sources at least up to $z \approx 3$. According to Figure 16(b), the 0.5–8 keV luminosity spans a very broad range (roughly six orders of magnitude) for both new and old sources; 13.6% of the main-catalog sources are very luminous (with $L_{0.5-8\ \mathrm{keV}} > 10^{44}$ erg s^{-1}; most are old sources), among which there are a number of sources that are highly obscured (see the upper right corner of Figure 16(c)). As seen in Figure 16(c), new sources could potentially have a similar range or distribution of band ratio to that of old sources, given that 82.7% of new sources have either lower limits (19.0%) or upper limits (81.0%) on their band ratios (see relevant discussions on this point later in this section).

Figure 17 shows distributions of observed-frame full-band flux (given in Column 74) and absorption-corrected, rest-frame 0.5–8 keV luminosity (given in Column 77) for new sources

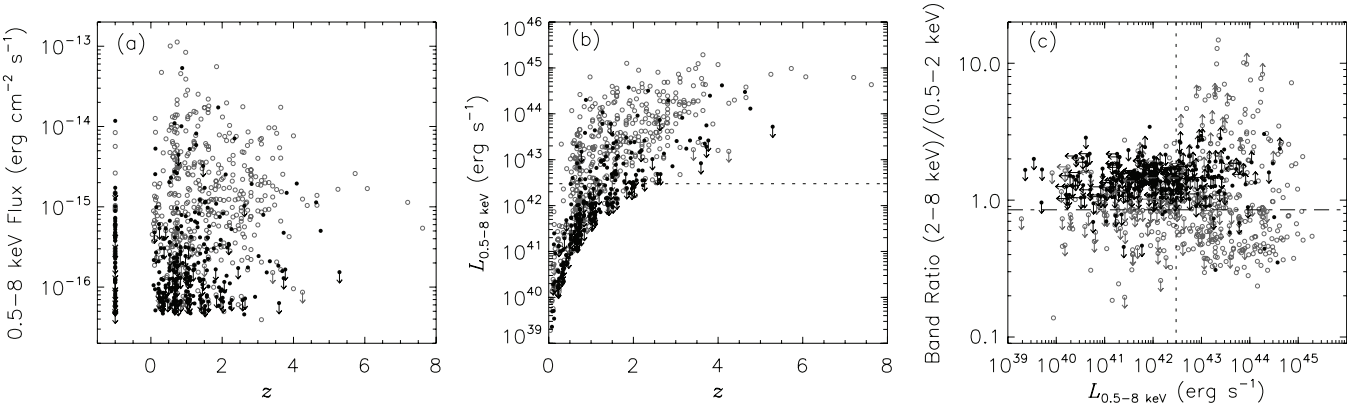

Figure 16. Plots of (a) observed-frame full-band flux vs. redshift, (b) absorption-corrected, rest-frame 0.5–8 keV luminosity vs. redshift, and (c) band ratio vs. absorption-corrected, rest-frame 0.5–8 keV luminosity, for the main-catalog sources. Gray open circles indicate the main-catalog sources that were previously detected in the L08 main catalog; black filled circles indicate the new main-catalog sources that were not previously detected in the L08 main catalog. Arrows indicate limits. Several sources shown in panels (a) and (b) have photometric redshifts greater than ≈4.5; these photometric redshifts are probably not very reliable due to poor photometric coverage (see Section 3.3 of L10 for more discussion). In panel (b), sources without redshift estimates have not been included in the plot; in panel (c), sources without redshift estimates and sources with only full-band detections have not been included in the plot. The dotted lines in panels (b) and (c) and the dash-dotted line in panel (c) indicate the threshold values of two AGN-identification criteria (i.e., $L_{0.5-8\ \mathrm{keV}} \geqslant 3 \times 10^{42}$ erg s^{-1} and $\Gamma \leqslant 1.0$; see the description of Column 78 for details).

(main panels) and old sources (insets), separated by source type. Based on our source-classification scheme, it is clear that sources with different types have disparate distributions of flux and luminosity when either new or old sources are considered, and that overall galaxies become the numerically dominant population at full-band fluxes less than $\approx 10^{-16}$ erg cm^{-2} s^{-1} or 0.5–8 keV luminosities less than $\approx 10^{42}$ erg s^{-1};[51] this trend is more pronounced when only new sources are considered. It is also clear that (1) new sources (either AGNs or galaxies) have similar ranges of flux and luminosity to those of old sources (either AGNs or galaxies); (2) new sources (either AGNs or galaxies), as expected, typically have smaller fluxes (i.e., have a smaller median flux) than old sources (either AGNs or galaxies); (3) compared to old AGNs, new AGNs typically have smaller luminosities (i.e., have a smaller median luminosity); and (4) compared to old galaxies, new galaxies have comparable luminosities (i.e., have about the same median luminosity).

We show in Figure 18(a) the band ratio as a function of full-band count rate for new sources (shown as filled symbols) and old sources (shown as open symbols). The sources are color-coded according to their likely types, with red, black, and blue colors indicating AGNs, galaxies, and stars, respectively. Also shown in Figure 18(a) are the average band ratios derived from stacking analyses following the procedure described in Luo et al. (2011), for all AGNs, all galaxies, and all sources (including both AGNs and galaxies), shown as large crosses, triangles, and diamonds, respectively. As expected, the overall average band ratio is dominated by AGNs because most of the main-catalog sources are AGNs and AGNs typically are more X-ray luminous than galaxies (see Figure 17). The overall average band ratio rises between full-band count rates of $\approx 10^{-2}$ and $\approx 10^{-4}$ counts s^{-1}, and it levels off and subsequently decreases below full-band count rates of $\approx 10^{-4}$ counts s^{-1}. The former increasing trend of the average band ratio is due to an increase

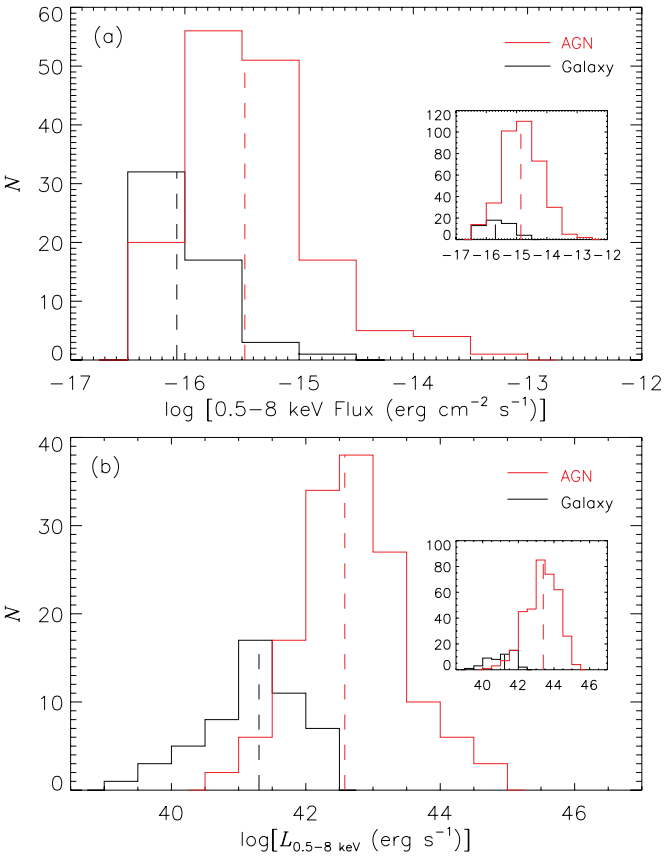

Figure 17. Distributions of (a) observed-frame full-band flux and (b) absorption-corrected, rest-frame 0.5–8 keV luminosity for the new main-catalog sources. The red and black histograms indicate AGNs and galaxies, respectively. The vertical red and black dashed lines indicate the median values for AGNs and galaxies, respectively. Sources with upper limits on full-band fluxes have not been included in the plotting for panel (a); sources without estimates of X-ray luminosities (due to no available redshift) or with upper limits on X-ray luminosities have not been included in the plotting for panel (b). The insets show results for the old main-catalog sources.

(A color version of this figure is available in the online journal.)

in the number of absorbed AGNs detected at fainter fluxes and has been reported previously (e.g., Tozzi et al. 2001; A03;

[51] There may be a selection effect that can potentially contribute to the result that galaxies numerically dominate over AGNs at $L_{0.5-8\ \mathrm{keV}} \lesssim 10^{42}$ erg s^{-1} since we used $L_{0.5-8\ \mathrm{keV}} \geqslant 3 \times 10^{42}$ erg s^{-1} as one of the AGN identification criteria. However, as shown in Section 4.4 (see the description of Column 78), ≳92% of the AGNs in the main catalog can be identified by the criteria other than the luminosity criterion; therefore, such a selection effect should be minimal.

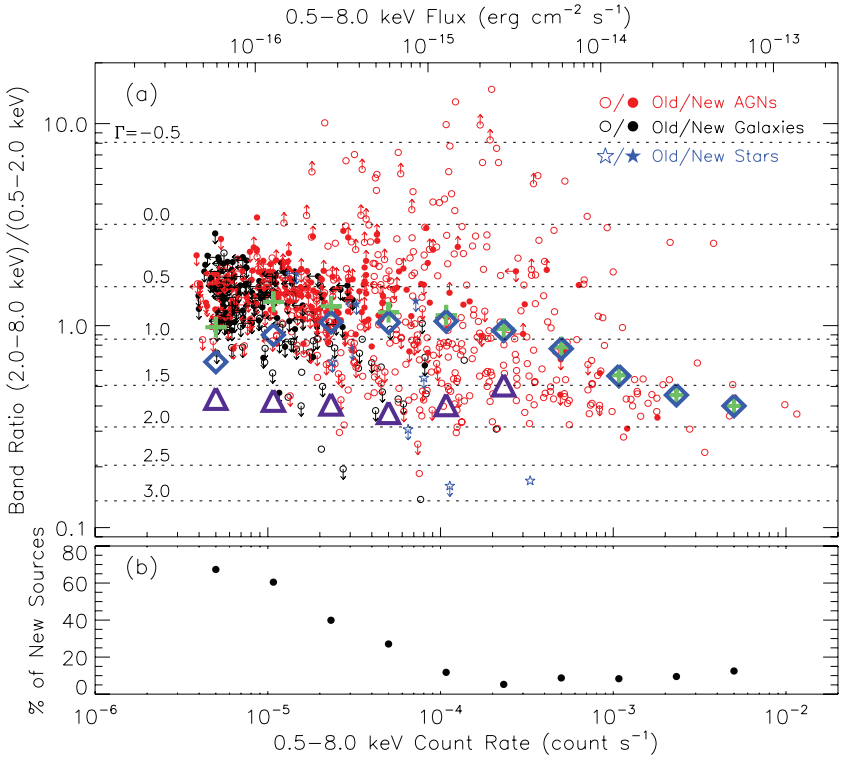

Figure 18. (a) Band ratio vs. full-band count rate for the main-catalog sources (for reference, the top x-axis shows representative full-band fluxes, which are derived from full-band count rates assuming a $\Gamma = 1.4$ power law). Sources that are considered AGNs, galaxies, and stars are colored red, black, and blue, respectively. Open circles and stars indicate AGNs/galaxies and stars that were previously detected in the L08 main catalog; filled circles and stars indicate new AGNs/galaxies and stars, respectively. Arrows indicate upper or lower limits, which mostly lie in the area of low count rates. Sources detected only in the full band cannot be plotted. Large crosses, triangles, and diamonds show average band ratios as a function of full-band count rate derived in bins of $\Delta\log(\text{Count Rate}) = 0.6$ from stacking analyses, for all AGNs, all galaxies, and all sources (including both AGNs and galaxies), respectively. Horizontal dotted lines show the band ratios corresponding to given effective photon indexes. (b) Fraction of new sources as a function of full-band count rate for the main-catalog sources. The fractions are calculated in bins of $\Delta\log(\text{Count Rate}) = 0.6$.

(A color version of this figure is available in the online journal.)

L05; L08); the latter decreasing trend of the average band ratio is partly because the contribution from normal and starburst galaxies increases at these lowest count rates (e.g., Bauer et al. 2004). Note that, at the lowest count rates studied, most of the sources have only band-ratio upper limits; thus the average band ratio lies below the individual-source upper limits. We show in Figure 18(b) the fraction of new sources as a function of full-band count rate for the main-catalog sources. Above full-band count rates of $\approx 10^{-4}$ counts s^{-1}, the fraction of new sources is small and roughly constant (≈5%–13%); below full-band count rates of $\approx 10^{-4}$ counts s^{-1}, the fraction of new sources rises from ≈12% to ≈67% toward smaller full-band count rates.

To examine further the band-ratio behavior of new and old sources, we show in Figure 19 the average (i.e., stacked) band ratio in bins of redshift and X-ray luminosity for new AGNs, old AGNs, new galaxies, and old galaxies, respectively. According to Figure 19, (1) new AGNs have larger band ratios than old AGNs no matter which bin of redshift or X-ray luminosity is considered (presumably due to the fact that the detection of highly absorbed AGNs with large band ratios requires deep observations given the small ACIS-I effective area at high energies); (2) in the two lower redshift bins ($0 < z < 1$ and $1 \leqslant z < 2$), the band ratios of new and old galaxies appear roughly consistent and constant within errors (hinting at no evolution in the X-ray spectral shape of the accreting binary populations that dominate the X-ray emission of normal and starburst galaxies); (3) new AGNs and old AGNs have similar patterns of band ratio versus X-ray luminosity, both peaking at the bin of $42.5 \leqslant \log(L_X) < 43.5$; and (4) in the lowest luminosity bin [$\log(L_X) < 41.5$], new galaxies have a larger average band ratio than old galaxies, while in a higher luminosity bin [$41.5 \leqslant \log(L_X) < 42.5$], new and old galaxies have consistent band ratios.

We show in Figure 20(a) the WFI R-band magnitude versus the full-band flux for new sources (filled symbols) and old sources (open symbols) as well as the approximate flux ratios for AGNs and galaxies (e.g., Maccacaro et al. 1988; Stocke et al. 1991; Hornschemeier et al. 2001; Bauer et al. 2004; also see the description of Column 78 for AGN identification). The sources are color-coded according to their likely types, with red, black, and blue colors indicating AGNs, galaxies, and stars, respectively. For comparison, we also show in Figure 20(c) the IRAC 3.6 μm magnitude versus the full-band flux for new sources (filled symbols) and old sources (open symbols), since a higher fraction of the main-catalog sources have counterparts in the IRAC 3.6 μm band than in the WFI R band (i.e., ≈88% versus ≈75%; see the description of Columns 23–43). Overall, a total of 568 (76.8%) of the main-catalog sources are likely AGNs, and the majority of them lie in the region expected for relatively luminous AGNs (i.e., $\log(f_X/f_R) > -1$; dark gray areas in Figure 20(a)); of these 568 AGNs, 192 (33.8%) are new. A total of 162 (21.9%) of the main-catalog sources are likely galaxies, and the majority of them lie in the region expected for normal galaxies, starburst galaxies, and low-luminosity AGNs (i.e., $\log(f_X/f_R) \leqslant -1$; light gray areas in Figure 20(a)); of these 162 sources, 104 (64.2%) are new. Only 10 (1.3%) of

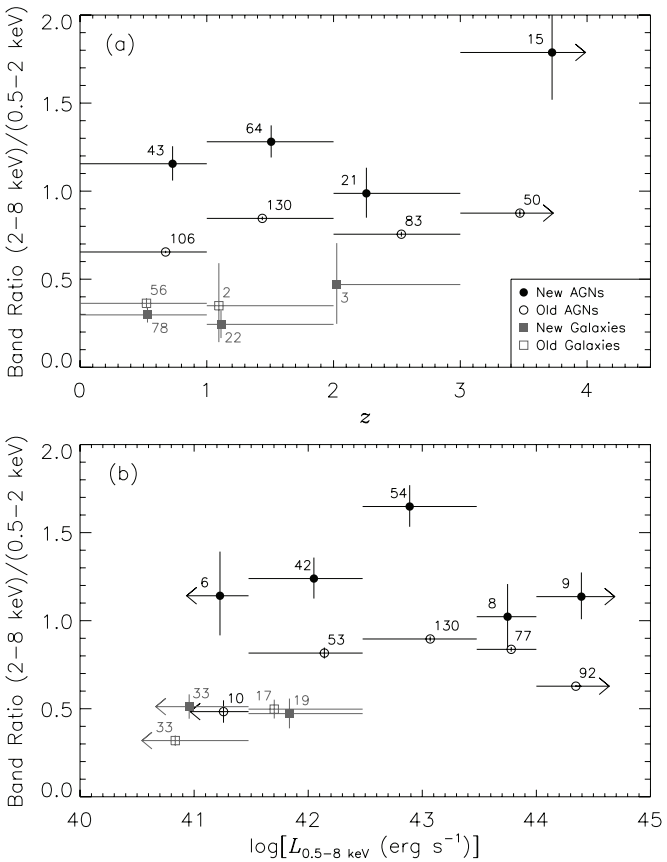

Figure 19. Average (i.e., stacked) band ratio in bins of (a) redshift ($0 < z < 1$, $1 \leqslant z < 2$, $2 \leqslant z < 3$, and $z \geqslant 3$) and (b) X-ray luminosity [$\log(L_X) < 41.5$, $41.5 \leqslant \log(L_X) < 42.5$, $42.5 \leqslant \log(L_X) < 43.5$, $43.5 \leqslant \log(L_X) < 44.0$, and $\log(L_X) \geqslant 44.0$] for new AGNs (filled circles), old AGNs (open circles), new galaxies (filled squares), and old galaxies (open squares). The median redshift or X-ray luminosity in each bin is used for plotting. The number of stacked sources in each redshift or luminosity bin is annotated.

the main-catalog sources are likely stars with low X-ray-to-optical flux ratios; of these 10 stars, 4 are new. Among new sources, normal and starburst galaxies account for a fraction of ≈35%, in contrast to ≈13% if old sources are considered. The above source-classification analysis indicates that, as expected, the 4 Ms CDF-S survey is detecting sources in or close to a regime where the galaxy number counts approach the AGN number counts, due to the steeper number-count slope expected for galaxies (e.g., Bauer et al. 2004).

Figure 21 shows the distributions of X-ray-to-optical flux ratio for new AGNs, old AGNs, new galaxies, and old galaxies, respectively. It is clear that (1) new AGNs generally have smaller X-ray-to-optical flux ratios than old AGNs and (2) new and old galaxies have similar distributions of X-ray-to-optical flux ratio.

5. SUPPLEMENTARY OPTICALLY BRIGHT *CHANDRA* SOURCE CATALOG

5.1. Supplementary-catalog Production

Of the 152 (i.e., 892 − 740 = 152) candidate-list X-ray sources that were not included in the main *Chandra* catalog (see Section 4.1), 119 were of moderate significance ($0.004 < P < 0.1$). To recover genuine X-ray sources from this sample, we constructed a supplementary *Chandra* source catalog consisting of the subset of these sources that have bright optical counterparts. Given that the density of optically bright sources on the sky is comparatively low, it is likely that the *Chandra* sources with such counterparts are real. We selected bright optical sources from the WFI *R*-band source catalog described in Section 3.1. We searched for bright optical counterparts (having $R \leqslant 24.0$) to the 119 X-ray sources of interest using a matching radius of 1.″2. The choices of $0.004 < P < 0.1$, the *R*-band cutoff magnitude, and the matching radius were made to ensure a good balance between the number of detected sources and the expected number of false sources. We find a total of 36 optically bright X-ray sources, of which 3 are L08 main-catalog sources that were not included in our main catalog and 3 are L08 supplementary optically bright sources (i.e., 30 new sources in the 4 Ms supplementary catalog). We note that the majority (22 out of 30) of the L08 supplementary optically bright sources are included in our main catalog (see the description of Column 59); this explains the small number of L08 supplementary sources included in our supplementary catalog. We estimated the expected number of false matches to be ≈2.2 (i.e., ≈6.1%) by manually shifting the X-ray source positions in right ascension and declination and recorrelating with the optical sources.

We present these 36 X-ray sources in Table 6 as a supplementary optically bright *Chandra* source catalog. The format of Table 6 is identical to that of Table 3 (see Section 4.4 for the details of each column). We note that the source-detection criterion is $P < 0.1$ for the sources in this supplementary catalog, as opposed to $P < 0.004$ for the main-catalog sources. Additionally, we set the multiwavelength identification-related columns (i.e., Columns 18–22) to the WFI *R*-band matching results.

5.2. Properties of Supplementary-catalog Sources

We show in Figure 15(b) the positions of the 36 sources in the supplementary optically bright *Chandra* catalog, with the 30 new sources shown as filled circles. These 36 supplementary sources have *R*-band AB magnitudes ranging from 15.1 to 23.9. We show in Figure 20(b) the *R*-band magnitude versus the full-band flux for these 36 sources, with the sources being color-coded based on their likely types. For comparison, Figure 20(d) shows the IRAC 3.6 μm magnitude versus the full-band flux for these 36 sources. A total of 12 (33.3%) of these 36 sources are likely AGNs; 22 (61.1%) of these 36 sources are likely galaxies and they all lie in the region expected for normal galaxies, starburst galaxies, and low-luminosity AGNs; 2 (5.6%) of these 36 sources are likely stars. The majority of these 36 supplementary sources appear to be optically bright, X-ray faint non-AGNs (e.g., A03; Hornschemeier et al. 2003) as a result of our selection criteria, and thus they are not representative of the faintest X-ray sources as a whole. A total of 31 (86.1%) of these 36 sources have either spectroscopic or photometric redshifts. Of the five sources that have no redshift estimate, two are bright stars with their redshifts set to −1.000; the other three have their photometry severely affected by a nearby bright source, thus no redshift estimates were available.

6. COMPLETENESS AND RELIABILITY ANALYSIS

We performed simulations to assess the completeness and reliability of our main catalog; such practice has been common among X-ray surveys (e.g., Cappelluti et al. 2007, 2009; Puccetti et al. 2009).

6.1. Generation of Simulated Data

First, we produced a mock catalog that covers the entire CDF-S and extends well below the detection limit of

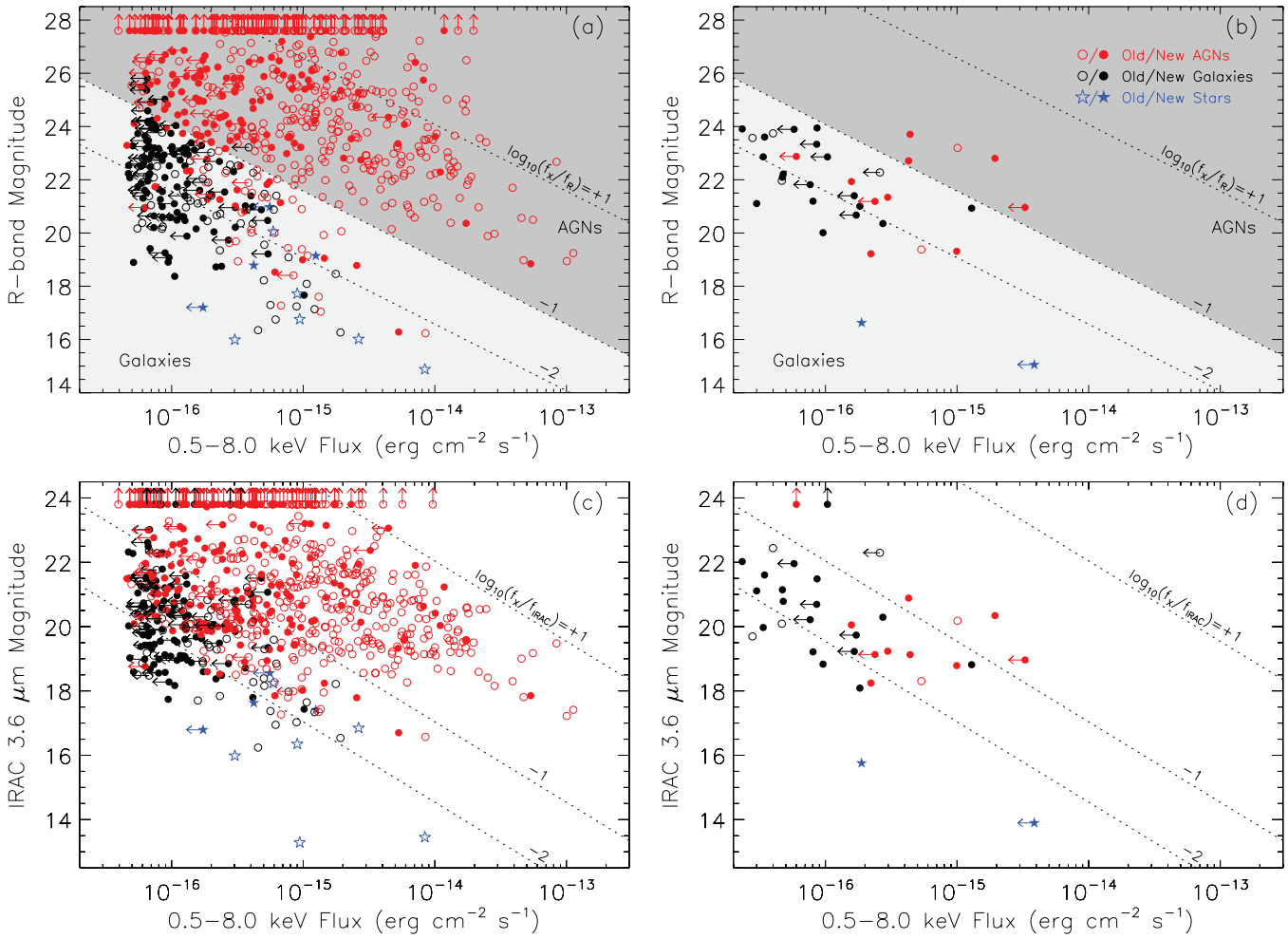

Figure 20. Top: WFI *R*-band magnitude vs. full-band flux for sources in (a) the main catalog and (b) the supplementary optically bright catalog (note that the legend in panel (b) applies for all the panels in this figure). Sources that are considered AGNs, galaxies, and stars are colored red, black, and blue, respectively. Open circles indicate AGNs/galaxies that were previously detected in (a) the L08 main catalog or (b) the L08 main or supplementary optically bright catalog; open stars in (a) indicate stars that were previously detected in the L08 main catalog; filled circles and stars indicate new AGNs/galaxies and stars, respectively. Arrows indicate limits. Diagonal lines indicate constant flux ratios between the WFI *R* band and the full band, with the shaded areas showing the approximate flux ratios for AGNs (dark gray) and galaxies (light gray). Bottom: IRAC 3.6 μm magnitude vs. full-band flux for sources in (c) the main catalog and (d) the supplementary optically bright catalog. All the symbols are the same as those in panels (a) and (b). The diagonal lines indicate constant flux ratios between the IRAC 3.6 μm band and the full band. Note that several galaxies that have *R*-band detections were not detected in the IRAC 3.6 μm band, probably due to source blending in the IRAC 3.6 μm band and/or these galaxies being very blue systems.

(A color version of this figure is available in the online journal.)

Table 6
Supplementary Optically Bright *Chandra* Source Catalog

	X-ray Coordinates		Detection Probability				Counts					
No.	α_{2000}	δ_{2000}	log P	WAVDETECT	Pos Err	Off-axis	FB	FB Upp Err	FB Low Err	SB	SB Upp Err	SB Low Err
(1)	(2)	(3)	(4)	(5)	(6)	(7)	(8)	(9)	(10)	(11)	(12)	(13)
1	03 31 44.64	−27 45 19.4	−1.9	−5	0.8	10.10	35.4	19.2	18.0	25.8	−1.0	−1.0
2	03 31 55.98	−27 39 42.8	−2.0	−5	1.1	11.25	24.2	14.1	12.9	14.6	8.1	6.9
3	03 31 56.42	−27 44 11.4	−1.9	−5	0.6	8.19	39.5	21.5	18.9	16.6	12.4	9.8
4	03 31 57.24	−27 45 37.2	−1.3	−5	0.8	7.38	64.8	−1.0	−1.0	16.7	11.5	10.3
5	03 32 07.63	−27 49 27.2	−2.3	−8	0.5	4.63	23.4	11.2	10.0	12.2	6.7	5.5

Notes. Units of right ascension are hours, minutes, and seconds, and units of declination are degrees, arcminutes, and arcseconds. The full table contains 79 columns of information for the 36 X-ray sources.

(This table is available in its entirety in a machine-readable form in the online journal. A portion is shown here for guidance regarding its form and content.)

the 4 Ms exposure (i.e., mock 0.5–2 keV flux limits of (2–3) $\times 10^{-18}$ erg cm^{-2} s^{-1}). Source coordinates were assigned using a recipe by Miyaji et al. (2007) to include realistic source clustering. In this mock catalog, each simulated AGN was assigned a soft-band flux that was drawn randomly from the soft-band log N–log S relation in the AGN population synthesis model by Gilli et al. (2007). Each simulated galaxy has a soft-band flux drawn randomly from the soft-band galaxy log N–log

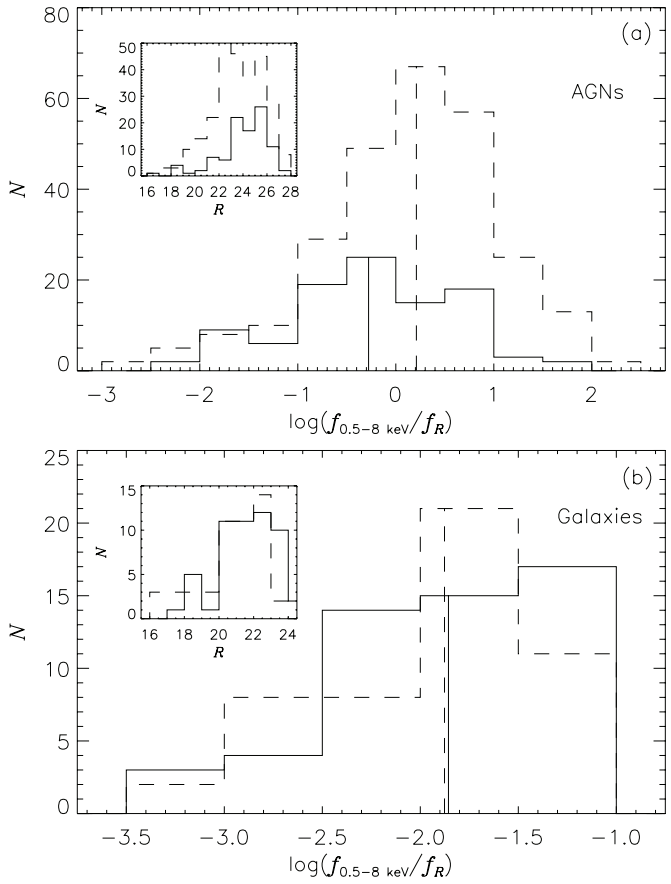

Figure 21. Distributions of X-ray-to-optical flux ratio for (a) new AGNs (solid histogram) and old AGNs (dashed histogram) and (b) new galaxies (solid histogram) and old galaxies (dashed histogram) with median flux ratios indicated by vertical lines. Shown in the insets are the distributions of *R*-band magnitude for new AGNs/galaxies (solid histograms) and old AGNs/galaxies (dashed histograms). Only sources with both full-band and *R*-band detections are shown.

S relation of the "peak-M" model by Ranalli et al. (2005). The AGN- and galaxy-integrated fluxes match the CXRB fluxes. The minimum soft-band fluxes simulated ($\approx 3 \times 10^{-18}$ erg cm^{-2} s^{-1} for AGNs and $\approx 2 \times 10^{-18}$ erg cm^{-2} s^{-1} for galaxies) are a factor of ≈3–5 below the detection limit of the central 4 Ms CDF-S (see Section 7.2); inclusion of these undetectable sources simulates the spatially non-uniform background component due to undetected sources. The soft-band fluxes of the simulated AGNs and galaxies were converted into full-band fluxes assuming power-law spectra with $\Gamma = 1.4$ and $\Gamma = 2.0$, respectively.

Second, we constructed event lists from 54 simulated ACIS-I observations of the mock catalog, each configured to have the same aim point, roll angle, exposure time, and aspect solution file as one of the CDF-S observations (see Table 1). The MARX simulator was used to convert source fluxes to a Poisson stream of dithered photons, and to simulate their detection by ACIS. These event lists represent only events arising from the mock point sources.

Third, we extracted the corresponding background event files that are appropriate to the simulated source event files from the real 4 Ms CDF-S event files. For each real event file, we masked all the events relevant to the main-catalog and supplementary-catalog sources and then filled the masked regions with events that obey the local probability distribution of background events. The resulting background event files include the contribution (≈0.5%) of unresolved faint sources that was also present in the MARX-simulated source event files. To avoid counting the contribution of unresolved faint sources twice, we removed 0.5% of the events at random in each background event file and then combined it with the corresponding source event file. Thus, we produced a set of 54 simulated ACIS-I observations that closely mirror the 54 real CDF-S observations.

Finally, we obtained a simulated merged event file (i.e., sum of source and background events) following Section 3.1, constructed images from this simulated merged event file for the three standard bands following Section 3.1, ran WAVDETECT on each simulated combined raw image at a false-positive probability threshold of 10^{-5} to produce a candidate-list catalog following Section 3.2, and utilized AE to perform photometry (and thus compute *P* values) for the sources in this candidate-list catalog following Section 3.2.

6.2. Completeness and Reliability

Our simulations allow us to assess the completeness and reliability of our main catalog. Completeness is defined as the ratio between the number of detected sources (given a specific detection criterion $P < P_0$) and the number of input simulated sources, above a specific source-count limit (this source-count limit applies to both the detected sources and the input simulated sources). Reliability is defined as 1 minus the ratio between the number of spurious sources and the number of input simulated sources, above a specific source-count limit (again, this source-count limit applies to both the spurious sources and the input simulated sources). The top panels of Figure 22 show the completeness and reliability as a function of the AE-computed binomial no-source probability *P* within the central $\theta \leqslant 6'$ area for the simulations in the full, soft, and hard bands, for sources with at least 15 counts and 8 counts. The bottom panels of Figure 22 correspond to the case for the entire CDF-S field. The case of 8 counts is close to our source-detection limit in the soft band. In each energy band, the completeness level for the case of 8 counts is, as expected, lower than that for the case of 15 counts, for both the central $\theta \leqslant 6'$ area and the entire CDF-S field; and the completeness level for the case of either 8 counts or 15 counts within the central $\theta \leqslant 6'$ area is higher than the corresponding completeness level in the entire CDF-S field. At the chosen main-catalog *P* threshold of 0.004, the completeness levels within the central $\theta \leqslant 6'$ area are 100.0% and 75.8% (full band), 100.0% and 94.1% (soft band), and 100.0% and 68.6% (hard band) for sources with at least 15 and 8 counts, respectively. The completeness levels for the entire CDF-S field are 82.4% and 49.3% (full band), 95.9% and 63.5% (soft band), and 74.7% and 47.6% (hard band) for sources with at least 15 and 8 counts, respectively. The reliability level ranges from 99.2% to 99.8% for each energy band and each source-count limit, which implies that, in the main catalog (i.e., the entire CDF-S field), there are about 4, 4, and 3 spurious detections with ⩾15 counts in the full, soft, and hard bands, and about 4, 5, and 3 spurious detections with ⩾8 counts in the full, soft, and hard bands, respectively.

We show in Figure 23 the completeness as a function of flux under the main-catalog $P < 0.004$ criterion for the simulations in the full, soft, and hard bands. These curves of completeness versus flux derived from the simulations approximately track the normalized sky coverage curves (i.e., the curves of survey solid angle versus flux limit; shown as solid curves in Figure 23) derived from the real CDF-S data (see Section 7.2). Table 7 gives the flux limits corresponding to four completeness levels in the

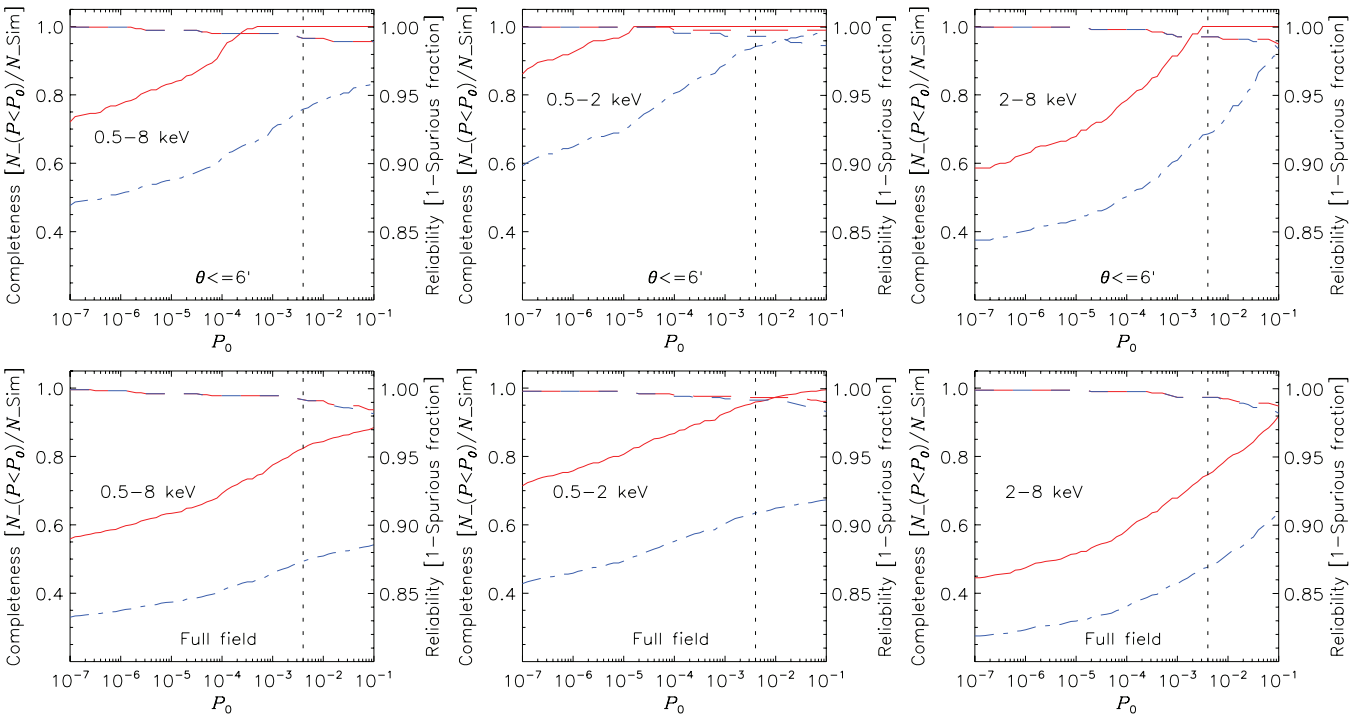

Figure 22. Top: case of $\theta \leqslant 6'$: completeness (solid and dash-dotted curves; left y-axis) and reliability (long dashed and short dashed curves; right y-axis) as a function of P_0, the AE-computed binomial no-source probability threshold chosen for detection, for the simulations in the full, soft, and hard bands, for sources with at least 15 counts (red solid and long dashed curves) and at least 8 counts (blue dash-dotted and short dashed curves), respectively. Note that the short dashed curves overlap almost exactly along the long dashed curves in some cases (e.g., top left and top right panels). The vertical dotted lines indicate the chosen main-catalog source-detection threshold of $P_0 = 0.004$. Bottom: same as top panels, but for the entire CDF-S field.

(A color version of this figure is available in the online journal.)

Table 7
Flux Limit and Completeness

Completeness (%)	$f_{0.5-8\ \mathrm{keV}}$ (erg cm^{-2} s^{-1})	$f_{0.5-2\ \mathrm{keV}}$ (erg cm^{-2} s^{-1})	$f_{2-8\ \mathrm{keV}}$ (erg cm^{-2} s^{-1})
90	2.8×10^{-15}	7.3×10^{-16}	4.0×10^{-15}
80	1.3×10^{-15}	3.5×10^{-16}	2.0×10^{-15}
50	3.0×10^{-16}	7.8×10^{-17}	4.6×10^{-16}
20	1.1×10^{-16}	2.9×10^{-17}	1.8×10^{-16}

full, soft, and hard bands, as shown as horizontal dotted lines in Figure 23.

7. BACKGROUND AND SENSITIVITY ANALYSIS

7.1. Background Map Creation

We created background maps for the three standard-band images as follows. We first masked the 740 main-catalog sources and the 36 supplementary-catalog sources using circular apertures with radii of 1.5 (2.0) times the ≈99% PSF EEF radii for sources with full-band counts below (above) 10,000. Larger masking radii were used for the brightest sources (there are three main-catalog sources with full-band counts above 10,000) to ensure that their source photons were fully removed. Approximately 18.3% of the pixels were masked. By design, the background maps include minimal or no contributions from the sources in the main and supplementary catalogs; however, the background in the regions of a few extended sources (e.g., Bauer et al. 2002; L05; A. Finoguenov et al. 2011, in preparation) will be slightly elevated. We then filled in the masked regions for each source with background counts that obey the local probability distribution of counts within an annulus with an inner radius being the aforementioned masking radius and an outer radius of 2.5 (3.0) times the ≈99% PSF EEF radius for sources with full-band counts below (above) 10,000. We summarize in Table 8 the background properties.

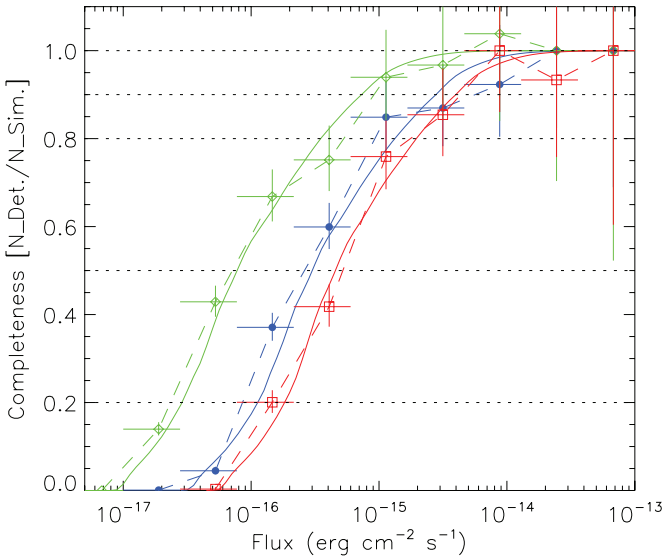

Figure 23. Completeness as a function of flux under the main-catalog $P < 0.004$ criterion for the simulations in the full (blue filled circles), soft (green open diamonds), and hard (red open squares) bands, overlaid with the corresponding sky coverage curves (solid curves) calculated in Section 7.3 and normalized to the maximum sky coverage (see the solid curves in Figure 25). The dashed lines connect the corresponding cross points. The horizontal dotted lines indicate five completeness levels.

(A color version of this figure is available in the online journal.)

Table 8
Background Parameters

Band (keV)	Mean Background		Total Background[c]	Count Ratio[d]
	(counts pixel^{-1})[a]	(counts Ms^{-1} pixel^{-1})[b]	(10^5 counts)	(Background/Source)
Full (0.5–8.0)	0.482	0.252	33.3	10.6
Soft (0.5–2.0)	0.119	0.063	8.2	4.3
Hard (2–8)	0.363	0.178	25.1	20.5

Notes.
[a] The mean numbers of background counts per pixel measured from the background maps (see Section 7.1; note that a pixel has a size of 0.″492), which were not corrected for vignetting or exposure-time variations.
[b] The mean numbers of counts per pixel divided by the mean effective exposures (i.e., 1.909 Ms, 1.877 Ms, and 2.040 Ms for the full band, soft band, and hard band, respectively) that are measured from the background maps (see Section 7.1) and exposure maps (see Section 3.1), respectively; these calculations take into account the effects of vignetting and exposure-time variations.
[c] Total numbers of background counts in the background maps.
[d] Ratio between the total number of background counts and the total number of detected source counts.

We find our mean background count rates to be in agreement with those presented in L08. Our background is the sum of contributions from the unresolved cosmic background, particle background, and instrumental background (e.g., Markevitch 2001; Markevitch et al. 2003). We do not distinguish between these different background contributions because we are here only interested in the total background. Even with a 4 Ms exposure, the majority of the pixels have no background counts; i.e., in the full, soft, and hard bands, ≈65%, 89%, and 72% of the pixels are zero, respectively.

7.2. Sensitivity Map Creation

According to Table 4, the minimum detected source counts are ≈11.4, 6.0, and 10.7 in the full, soft, and hard bands for the main-catalog sources, which correspond to full, soft, and hard-band fluxes of $\approx 3.5 \times 10^{-17}$, 8.8×10^{-18}, and 6.4×10^{-17} erg cm^{-2} s^{-1}, respectively, assuming that sources having these minimum counts are located at the average aim point and have a $\Gamma = 1.4$ power-law spectrum with Galactic absorption. This calculation provides a measure of the ultimate sensitivity of the main catalog, which, however, is only relevant for a small central region near the average aim point. We created sensitivity maps in the three standard bands for the main catalog in order to determine the sensitivity as a function of position across the field.

In the binomial no-source probability equation (i.e., Equation (1) in Section 4.1), we need to measure $B_{\rm src}$ and $B_{\rm ext}$ to obtain the minimum number of counts required for a detection (S), given the criterion of $P_{\rm threshold} = 0.004$. We determined $B_{\rm src}$ in the background maps for the main catalog using circular apertures with ≈90% PSF EEF radii. Due to the PSF broadening with off-axis angle, the value of $B_{\rm ext}$ has an off-axis angle dependency, i.e., the larger the off-axis angle, the larger the value of $B_{\rm ext}$. To follow the behavior of AE when extracting background counts of the main-catalog sources, we derived the value of $B_{\rm ext}$ as follows: for a given pixel in the background map, we computed its off-axis angle θ_p and set the value of $B_{\rm ext}$ to the maximum $B_{\rm ext}$ value of the main-catalog sources that are located in an annulus with the inner/outer radius being $\theta_p - 0.'25$/$\theta_p + 0.'25$ (note that the adopted maximum $B_{\rm ext}$ value corresponds to the highest sensitivity). Given the computed $B_{\rm src}$ and $B_{\rm ext}$, we numerically solved Equation (1) to obtain the minimum counts S (in the source-extraction region) required for detections under the main-catalog source-detection criterion $P < 0.004$. We then created sensitivity maps for the main catalog using the exposure maps, assuming a $\Gamma = 1.4$ power-law model with Galactic absorption. The above procedure takes into account effects such as the PSF broadening with off-axis angle, the varying effective exposure (due to, e.g., vignetting and CCD gaps; see Figure 2), and the varying background rate across the field. There are 11 main-catalog sources lying ≈1%–9% below the derived sensitivity limits, i.e., 5 sources in the full band, 6 sources in the soft band, and none in the hard band, probably due to background fluctuations and/or their real Γ values deviating significantly from the assumed value.

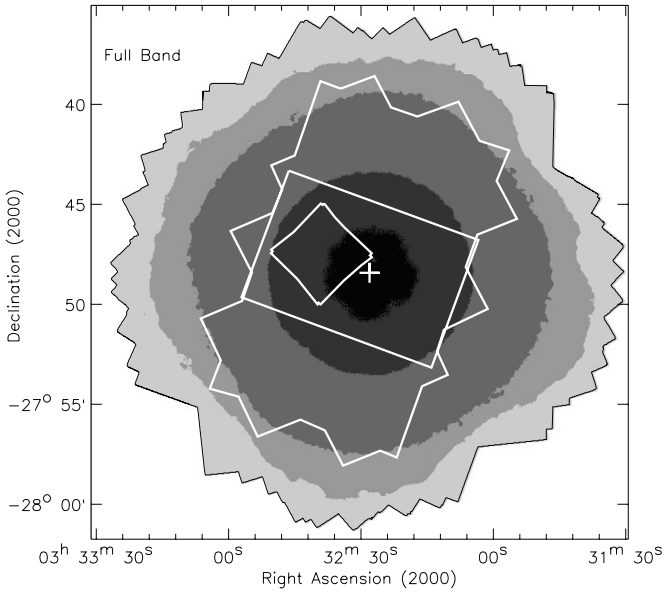

Figure 24. Full-band sensitivity map for the main catalog, created following Section 7.2. The gray-scale levels, from black to light gray, represent areas with flux limits of $<4.0 \times 10^{-17}$, 4.0×10^{-17} to 10^{-16}, 10^{-16} to 3.3×10^{-16}, 3.3×10^{-16} to 10^{-15}, and $>10^{-15}$ erg cm^{-2} s^{-1}, respectively. The regions and the plus sign are the same as those in Figure 1.

We show in Figure 24 the full-band sensitivity map for the main catalog. It is apparent that higher sensitivities are achieved at smaller off-axis angles. The ≈1 arcmin^2 region at the average aim point has mean sensitivity limits of $\approx 3.2 \times 10^{-17}$, 9.1×10^{-18}, and 5.5×10^{-17} erg cm^{-2} s^{-1} for the full, soft, and hard bands, respectively.

7.3. Sensitivities of and Prospects for Longer Chandra Exposures

To investigate the improvement in sensitivity due to additional exposure, we also created exposure maps, background maps, and

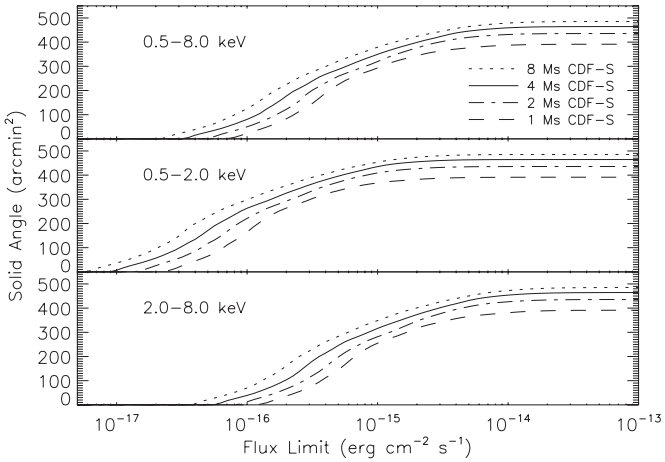

Figure 25. Survey solid angle as a function of flux limit in the three standard bands for the main catalog (shown as solid curves), determined following Section 7.2. For comparison, the curves for the 1 Ms CDF-S (shown as dashed curves), the 2 Ms CDF-S (shown as dash-dotted curves), and the simulated 8 Ms CDF-S (shown as dotted curves) are also plotted; these curves are calculated/simulated consistently (see Section 7.3).

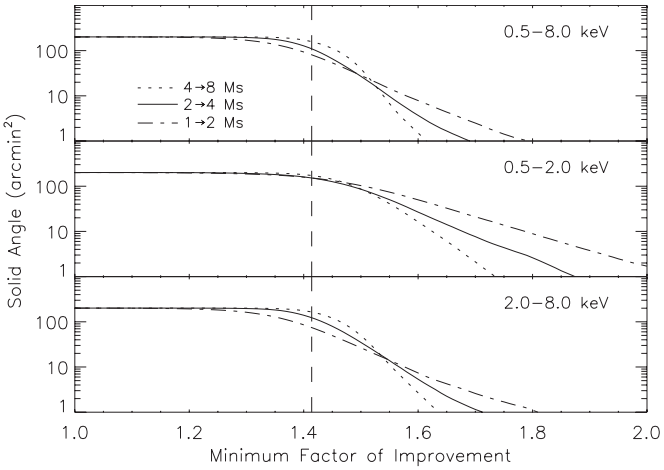

Figure 26. Survey solid angle within the central $\theta = 8'$ area as a function of minimum factor of improvement in sensitivity in the three standard bands under the source-detection criterion $P < 0.004$. The improvement curves for the cases of 1–2 Ms, 2–4 Ms, and 4–8 Ms are shown as dash-dotted, solid, and dotted curves, respectively; the curves for the first two cases are calculated using real data, while the curves for the third case are simulated (see Section 7.3). The vertical dashed lines indicate a factor of $\sqrt{2}$ improvement in sensitivity that is expected for each doubling of exposure time in a background-limited case under the assumption, here inapplicable, of Gaussian statistics.

sensitivity maps for the 1 Ms and 2 Ms CDF-S and simulated exposure maps, background maps, and sensitivity maps for the 8 Ms CDF-S. We followed the procedure detailed in Section 3.1 to create exposure maps for the 1 Ms and 2 Ms CDF-S. We simulated the 8 Ms CDF-S exposure maps by rotating the 4 Ms CDF-S exposure maps 90 deg clockwise about the average aim point (this rotation approach simulates the variations of roll angles between observations) and then adding the rotated 4 Ms exposure maps to the real 4 Ms exposure maps. We followed Section 7.1 to create background maps for the 1 Ms and 2 Ms CDF-S. To obtain the 8 Ms CDF-S background maps, we first simulated a set of 4 Ms CDF-S background maps by filling in each pixel in a simulated background map with background counts that obey the local probability distribution of counts derived from the corresponding real 4 Ms CDF-S background map; we then rotated the simulated 4 Ms background maps 90 deg clockwise about the average aim point and added the rotated 4 Ms background maps to the real 4 Ms background maps. We followed the procedure detailed in Section 7.2 to create sensitivity maps for the 1 Ms, 2 Ms, and 8 Ms CDF-S under the source-detection criterion $P < 0.004$, where we appropriately scaled the value of $B_{\rm ext}$ that was derived when creating the 4 Ms sensitivity maps (i.e., scaling factors of 0.25, 0.50, and 2.0 were adopted for the 1 Ms, 2 Ms, and 8 Ms CDF-S, respectively).

We show in Figure 25 plots of solid angle versus flux limit in the three standard bands for the 1–8 Ms CDF-S under the source-detection criterion $P < 0.004$. It is clear that, for each of the three standard bands, the quantitative increases in sensitivity are comparable between the cases of 1–2 Ms, 2–4 Ms, and 4–8 Ms. To examine the improvement in sensitivity more clearly, we created sensitivity improvement maps by dividing the 1 Ms, 2 Ms, and 4 Ms sensitivity maps by the 2 Ms, 4 Ms, and 8 Ms sensitivity maps, respectively. We show in Figure 26 plots of solid angle versus minimum factor of improvement in sensitivity in the three standard bands between the 1 Ms, 2 Ms, and 4 Ms CDF-S and the 2 Ms, 4 Ms, and 8 Ms CDF-S, respectively. Figure 26 only considers the central $\theta = 8'$ area, since such an area will be covered by any individual CDF-S observation. It is clearly shown in Figure 26 that (1) for the three standard bands, the majority of the central CDF-S area generally has a factor of $>\sqrt{2}$ improvement in sensitivity for each doubling of exposure time (note that $\sqrt{2} = 1.414$ corresponds to the background-limited case under the assumption, here inapplicable, of Gaussian statistics); and (2) among the three standard bands, the improvement in sensitivity is most pronounced in the soft band for each doubling of exposure time, due to the fact that the soft band has the lowest background level (see, e.g., Table 8). We note that, for each of the three standard bands during each doubling of exposure time, the improvement in sensitivity greater than a factor of 1.5–1.6 generally occurs in the ACIS-I CCD gap areas (see Figure 2) where the improvement in exposure time is often greater than a factor of two. For the central $\approx$100 arcmin^2 area, the average improvement in sensitivity is typically a factor of 1.4–1.6 for each of the three standard bands, no matter which case of 1–2 Ms, 2–4 Ms, or 4–8 Ms is considered. Based on the above analyses, we conclude that additional exposure over the CDF-S region, e.g., doubling the current 4 Ms exposure, will still yield higher sensitivities in the central area of the field by a comparable amount to any previous doubling of exposure time (i.e., 1–2 Ms or 2–4 Ms). The faintest sources detected in an 8 Ms CDF-S should have full-, soft-, and hard-band fluxes of $\approx 2.1 \times 10^{-17}$, 6.0×10^{-18}, and 3.7×10^{-17} erg cm^{-2} s^{-1}, respectively. Based upon the derived sensitivity maps and CXRB synthesis models (e.g., Gilli et al. 2007; Treister et al. 2009), a total of $\approx$1000 sources, including $\approx$120–130 new AGNs and $\approx$90–100 new galaxies, are expected to be detected in an 8 Ms CDF-S.

In addition to the improvements in sensitivity described above that would probe unexplored discovery space, significant additional CDF-S exposure could greatly improve the X-ray spectra, light curves, and positions for the nearly 800 known X-ray sources in our main and supplementary catalogs. This would provide improved physical understanding of these sources; e.g., AGN content and luminosity, level and nature of AGN obscuration, shape of the X-ray continuum, and level of X-ray emission from X-ray binaries and supernova remnants.

8. SUMMARY

We have presented catalogs and basic analyses of X-ray sources detected in the deepest *Chandra* survey: the 4 Ms CDF-S. We summarize the most-important results as follows.

1. The entire CDF-S consists of 54 individual observations, with a summed exposure of 3.872 Ms and a total solid angle coverage of 464.5 arcmin^2.
2. The main *Chandra* source catalog contains 740 sources that were detected with WAVDETECT at a false-positive probability threshold of 10^{-5} and satisfy our binomial-probability source-selection criterion of $P < 0.004$; this approach is designed to maximize the number of reliable sources detected. These 740 sources were detected in up to three standard X-ray bands: 0.5–8.0 keV (full band), 0.5–2.0 keV (soft band), and 2–8 keV (hard band). Seven hundred sixteen (96.8%) of these 740 sources have multiwavelength counterparts, with 673 (94.0% of 716) having either spectroscopic or photometric redshifts.
3. The supplementary *Chandra* source catalog consists of 36 sources that were detected with WAVDETECT at a false-positive probability threshold of 10^{-5} and satisfy the conditions of having $0.004 < P < 0.1$ and having bright optical counterparts ($R < 24.0$).
4. X-ray source positions for the main and supplementary *Chandra* source catalogs have been determined using centroid and matched-filter techniques. The absolute astrometry of the combined X-ray images and X-ray source positions has been established using a VLA 1.4 GHz radio catalog. The median positional uncertainty at the ≈68% confidence level is 0.″42/0.″72 for the main/supplementary *Chandra* source catalog.
5. Basic analyses of the X-ray and optical properties of the sources indicate that they represent a variety of source types. More than 75% of the sources in the main *Chandra* catalog are likely AGNs. Near the center of the 4 Ms CDF-S (i.e., within an off-axis angle of 3′), the observed AGN and galaxy source densities have reached 9800^{+1300}_{-1100} deg^{-2} and 6900^{+1100}_{-900} deg^{-2}, respectively. The majority of the sources in the supplementary optically bright catalog are likely normal and starburst galaxies.
6. A total of 300 main-catalog sources are new, compared to the 2 Ms main-catalog sources. Of the 300 new main-catalog sources, ≈64% are likely AGNs while ≈35% are likely normal and starburst galaxies (the remaining ≈1% are likely stars), reflecting the rise of normal and starburst galaxies at these very faint fluxes. Indeed, based on our source-classification scheme, galaxies become the numerically dominant population of sources appearing at 0.5–8 keV fluxes less than $\approx 10^{-16}$ erg cm^{-2} s^{-1} or luminosities less than $\approx 10^{42}$ erg s^{-1}.
7. Simulations show that our main catalog is highly reliable (e.g., $\lesssim$5 spurious detections are expected in the soft band) and is reasonably complete (e.g., the completeness level for the soft band is >94% for sources with $\geqslant$8 counts in the central $\theta \leqslant 6'$ area).
8. The mean background (corrected for vignetting and exposure-time variations) is 0.252, 0.063, and 0.178 counts Ms^{-1} pixel^{-1} for the full, soft, and hard bands, respectively; the majority of the pixels have zero background counts.
9. The 4 Ms CDF-S reaches on-axis flux limits of $\approx 3.2 \times 10^{-17}$, 9.1×10^{-18}, and 5.5×10^{-17} erg cm^{-2} s^{-1} for the full, soft, and hard bands, respectively, a factor of 1.5–1.6 improvement over the 2 Ms CDF-S. Another doubling of the CDF-S exposure time would still yield higher sensitivities in the central area of the field by a comparable amount to any previous doubling of exposure time, thus providing a significant number of new X-ray sources that probe the key unexplored discovery space.

The CDF-S source catalogs and data products provided by this paper will be beneficial to many ongoing and future studies; e.g., a search for a population of heavily obscured AGNs at intermediate redshifts (Luo et al. 2011), X-ray spectral constraints on heavily obscured and Compton-thick AGNs at high redshifts (Alexander et al. 2011; Gilli et al. 2011), derivation of X-ray number counts for different source types and the evolution of normal-galaxy luminosity functions (B. D. Lehmer et al. 2011, in preparation), and a study of extended sources (A. Finoguenov et al. 2011, in preparation). The CDF-S will continue to be a premiere deep-survey field over the coming decades; the CDF-S imaging and spectroscopic coverage are superb and continue to improve. For example, CANDELS[52] will utilize *HST*/WFC3 to image the GOODS-S; the highest sensitivity will be achieved with 5-orbit observations in the central region of this field. Together, deeper *Chandra* and multiwavelength data will be critical to allow comprehensive understanding of faint X-ray sources.

We thank the referee for helpful feedback that improved this work. We thank the *Chandra* Director's Office for allocating the time for these observations. We also thank L. K. Townsley for helpful discussions on data reduction and N. A. Miller for kindly providing the 5σ VLA 1.4 GHz radio catalog. Support for this work was provided by NASA through *Chandra* Award SP1-12007A (Y.Q.X., B.L., W.N.B., F.E.B.) issued by the *Chandra* X-ray Observatory Center, which is operated by the Smithsonian Astrophysical Observatory, and by NASA ADP grant NNX10AC996 (Y.Q.X., B.L., W.N.B.). We also acknowledge the financial support of the Chile CONICYT under grants FONDECYT 1101024 and FONDAP (CATA) 15010003 (F.E.B.), the Royal Society (D.M.A.), the Philip Leverhulme Prize (D.M.A.), the Science and Technology Facilities Council (D.M.A., IRS), the Italian Space Agency (ASI) under the ASI-INAF contracts I/009/10/0 and I/088/06/0 (A.C., R.G., P.T., C.V.), and the German Deutsche Forschungsgemeinschaft Leibniz Prize FKZ HA 1850/28-1 (G.H.).

REFERENCES

Alexander, D. M., Bauer, F. E., Chapman, S. C., Smail, I., Blain, A. W., Brandt, W. N., & Ivison, R. J. 2005, ApJ, 632, 736
Alexander, D. M., Brandt, W. N., Hornschemeier, A. E., Garmire, G. P., Schneider, D. P., Bauer, F. E., & Griffiths, R. E. 2001, AJ, 122, 2156
Alexander, D. M., et al. 2003, AJ, 126, 539 (A03)
Alexander, D. M., et al. 2011, ApJ, in press (arXiv:1106.1443)
Baganoff, F. K., et al. 2003, ApJ, 591, 891
Balestra, I., et al. 2010, A&A, 512, 12
Bauer, F. E., Alexander, D. M., Brandt, W. N., Schneider, D. P., Treister, E., Hornschemeier, A. E., & Garmire, G. P. 2004, AJ, 128, 2048
Bauer, F. E., et al. 2002, AJ, 123, 1163
Beckwith, S. V. W., et al. 2006, AJ, 132, 1729
Boller, T., Bertoldi, F., Dennefeld, M., & Voges, W. 1998, A&AS, 129, 87
Brandt, W. N., & Alexander, D. M. 2010, Pub. Natl Acad. Sci., 107, 7184
Brandt, W. N., & Hasinger, G. 2005, ARA&A, 43, 827
Broos, P. S., Feigelson, E. D., Townsley, L. K., Getman, K. V., Wang, J., Garmire, G. P., Jiang, Z., & Tsuboi, Y. 2007, ApJS, 169, 353

[52] See http://candels.ucolick.org/index.html for details on CANDELS.

Broos, P. S., Townsley, L. K., Feigelson, E. D., Getman, K. V., Bauer, F. E., & Garmire, G. P. 2010, ApJ, 714, 1582
Broos, P. S., et al. 2000, User's Guide for the TARA Package (University Park, PA: Pennsylvania State Univ.; http://www.astro.psu.edu/xray/docs/TARA/TARA_users_guide)
Broos, P. S., et al. 2011, ApJS, 194, 2
Brusa, M., et al. 2005, A&A, 432, 69
Brusa, M., et al. 2007, ApJS, 172, 353
Caldwell, J. A. R., et al. 2008, ApJS, 174, 136
Cappelluti, N., et al. 2007, ApJS, 172, 341
Cappelluti, N., et al. 2009, A&A, 497, 635
Cardamone, C. N., et al. 2010, ApJS, 189, 270
Ciliegi, P., Zamorani, G., Hasinger, G., Lehmann, I., Szokoly, G., & Wilson, G. 2003, A&A, 398, 901
Comastri, A., et al. 2011, A&A, 526, L9
Damen, M., et al. 2011, ApJ, 727, 1
Eadie, W. T., Dryard, D., James, F. E., Roos, M., & Sadoulet, B. 1971, Statistical Methods in Experimental Physics (Amsterdam: North-Holland)
Ebeling, H., White, D. A., & Rangarajan, F. V. N. 2006, MNRAS, 368, 65
Feldmann, R., et al. 2006, MNRAS, 372, 565
Freeman, P. E., Kashyap, V., Rosner, R., & Lamb, D. Q. 2002, ApJS, 138, 185
Garmire, G. P., Bautz, M. W., Ford, P. G., Nousek, J. A., & Ricker, G. R., Jr. 2003, Proc. SPIE, 4851, 28
Gehrels, N. 1986, ApJ, 303, 336
Gendreau, K. C., et al. 1995, PASJ, 47, L5
Georgakakis, A., Nandra, K., Laird, E. S., Aird, J., & Trichas, M. 2008, MNRAS, 388, 1205
Getman, K. V., et al. 2005, ApJS, 160, 319
Giacconi, R., et al. 2002, ApJS, 139, 369
Giavalisco, M., et al. 2004, ApJ, 600, L93
Gilli, R., Comastri, A., & Hasinger, G. 2007, A&A, 463, 79
Gilli, R., et al. 2011, ApJ, 730, L28
Grazian, A., et al. 2006, A&A, 449, 951
Hasinger, G., Burg, R., Giacconi, R., Schmidt, M., Trumper, J., & Zamorani, G. 1998, A&A, 329, 482
Hickox, R. C., & Markevitch, M. 2006, ApJ, 645, 95
Hornschemeier, A. E., et al. 2001, ApJ, 554, 742
Hornschemeier, A. E., et al. 2003, AJ, 126, 575
Hornschemeier, A. E., et al. 2004, ApJ, 600, 147
Kim, M., et al. 2007, ApJS, 169, 401
Komatsu, E., et al. 2011, ApJS, 192, 18
Kraft, R. P., Burrows, D. N., & Nousek, J. A. 1991, ApJ, 374, 344
Laird, E. S., et al. 2009, ApJS, 180, 102
Le Fèvre, O., et al. 2004, A&A, 428, 1043
Lehmer, B. D., Brandt, W. N., Hornschemeier, A. E., Alexander, D. M., Bauer, F. E., Koekemoer, A. M., Schneider, D. P., & Steffen, A. T. 2006, AJ, 131, 2394
Lehmer, B. D., et al. 2005, ApJS, 161, 21 (L05)
Lehmer, B. D., et al. 2008, ApJ, 681, 1163
Lehmer, B. D., et al. 2009, MNRAS, 400, 299
Luo, B., et al. 2008, ApJS, 179, 19 (L08)
Luo, B., et al. 2010, ApJS, 187, 560 (L10)
Luo, B., et al. 2011, ApJ, submitted
Lyons, L. 1991, Data Analysis for Physical Science Students (Cambridge: Cambridge Univ. Press)
Maccacaro, T., Gioia, I. M., Wolter, A., Zamorani, G., & Stocke, J. T. 1988, ApJ, 326, 680
Markevitch, M. 2001, CXC Memo (Cambridge: CXC), http://cxc.harvard.edu/cal/calreview/mm_calrev_bg.ps
Markevitch, M., et al. 2003, ApJ, 583, 70
Marshall, F. E., Boldt, E. A., Holt, S. S., Miller, R. B., Mushotzky, R. F., Rose, L. A., Rothschild, R. E., & Serlemitsos, P. J. 1980, ApJ, 235, 4
Mignoli, M., et al. 2005, A&A, 437, 883
Miller, N. A., Fomalont, E. B., Kellermann, K. I., Mainieri, V., Norman, C., Padovani, P., Rosati, P., & Tozzi, P. 2008, ApJS, 179, 114
Miyaji, T., et al. 2007, ApJS, 172, 396
Nandra, K., et al. 2005, MNRAS, 356, 568
Oke, J. B., & Gunn, J. E. 1983, ApJ, 266, 713
Paolillo, M., Schreier, E. J., Giacconi, R., Koekemoer, A. M., & Grogin, N. A. 2004, ApJ, 611, 93
Popesso, P., et al. 2009, A&A, 494, 443
Puccetti, S., et al. 2009, ApJS, 185, 586
Rafferty, D. A., et al. 2011, ApJ, submitted
Ranalli, P., Comastri, A., & Setti, G. 2005, A&A, 440, 23
Ravikumar, C. D., et al. 2007, A&A, 465, 1099
Retzlaff, J., et al. 2010, A&A, 511, 50
Santini, P., et al. 2009, A&A, 504, 751
Silverman, J. D., et al. 2010, ApJS, 191, 124
Stark, A. A., Gammie, C. F., Wilson, R. W., Bally, J., Linke, R. A., Heiles, C., & Hurwitz, M. 1992, ApJS, 79, 77
Stocke, J. T., Morris, S. L., Gioia, I. M., Maccacaro, T., Schild, R., Wolter, A., Fleming, T. A., & Henry, J. P. 1991, ApJS, 76, 813
Sutherland, W., & Saunders, W. 1992, MNRAS, 259, 413
Szokoly, G. P., et al. 2004, ApJS, 155, 271
Taylor, E. N., et al. 2009, ApJS, 183, 295
Townsley, L. K., Broos, P. S., Garmire, G. P., & Nousek, J. A. 2000, ApJ, 534, L139
Townsley, L. K., Broos, P. S., Nousek, J. A., & Garmire, G. P. 2002, Nucl. Instrum. Methods Phys. Res. A, 486, 751
Tozzi, P., et al. 2001, ApJ, 562, 42
Treister, E., Urry, C. M., & Virani, S. 2009, ApJ, 696, 110
Treister, E., et al. 2009, ApJ, 693, 1713
Vanzella, E., et al. 2008, A&A, 478, 83
Vikhlinin, A. 2001, Reducing ACIS Quiescent Background Using Very Faint Mode (Cambridge: CXC; http://cxc.harvard.edu/cal/Acis/Cal_prods/vfbkgrnd/)
Vikhlinin, A., Forman, W., Jones, C., & Murray, S. 1995, ApJ, 451, 553
Weisskopf, M. C., Wu, K., Trimble, V., O'Dell, S. L., Elsner, R. F., Zavlin, V. E., & Kouveliotou, C. 2007, ApJ, 657, 1026
Xue, Y. Q., et al. 2010, ApJ, 720, 368
Zheng, W., et al. 2004, ApJS, 155, 73